

# Scalable manifold learning by uniform landmark sampling and constrained locally linear embedding

Dehua Peng<sup>1, 2, 3, \*</sup>, Zhipeng Gui<sup>2, 3, \*</sup>, Wenzhang Wei<sup>2</sup> and Huayi Wu<sup>1, 3</sup>

<sup>1</sup>State Key Laboratory of Information Engineering in Surveying, Mapping and Remote Sensing, Wuhan University, Wuhan 430079, China.

<sup>2</sup>School of Remote Sensing and Information Engineering, Wuhan University, Wuhan 430079, China.

<sup>3</sup>Collaborative Innovation Center of Geospatial Technology, Wuhan University, Wuhan 430079, China.

\*Correspondence to: Email: {pengdh; zhipeng.gui}@whu.edu.cn

**Abstract:** As a pivotal approach in machine learning and data science, manifold learning aims to uncover the intrinsic low-dimensional structure within complex nonlinear manifolds in high-dimensional space. By exploiting the manifold hypothesis, various techniques for nonlinear dimension reduction have been developed to facilitate visualization, classification, clustering, and gaining key insights. Although existing manifold learning methods have achieved remarkable successes, they still suffer from extensive distortions incurred in the global structure, which hinders the understanding of underlying patterns. Scalability issues also limit their applicability for handling large-scale data. Here, we propose a scalable manifold learning (scML) method that can manipulate large-scale and high-dimensional data in an efficient manner. It starts by seeking a set of landmarks to construct the low-dimensional skeleton of the entire data and then incorporates the non-landmarks into the landmark space based on the constrained locally linear embedding (CLLE). We empirically validated the effectiveness of scML on synthetic datasets and real-world benchmarks of different types, and applied it to analyze the single-cell transcriptomics and detect anomalies in electrocardiogram (ECG) signals. scML scales well with increasing data sizes and exhibits promising performance in preserving the global structure. The experiments demonstrate notable robustness in embedding quality as the sample rate decreases.

## Main

Dimension reduction plays an indispensable role in both preprocessing for machine learning tasks and visualization for high-dimensional data [1, 2]. It is often applied to address the curse of dimensionality in data science, which refers to the phenomenon where the amount of data required to achieve a certain level of accuracy increases exponentially as the number of dimensions increases [3]. This makes models difficult to represent the features comprehensively and may lead to an overfitting problem [4]. By reducing the worthless and redundant features, dimension reduction not only improves the time efficiency of data analysis but also enhances the generalization ability and interpretability of models. Additionally, dimension reduction is a fundamental visualizing technique for high-dimensional data, enabling users to gain the underlying group patterns and pairwise relationships in the data. As the most classical dimension reduction methods, principal component analysis (PCA) [5] and multidimensional scaling (MDS) [6] are widely applied in many fields due to their concise theories, remarkable performance, and strong adaptability. PCA finds the direction of maximum variance and projects the data into a lower-dimensional space spanned by the principal components [7], while MDS minimizes the differences between pairwise distances in the original

and embedded space. However, they neglect the inter-cluster separation and tend to cause a crowding problem. Therefore, linear discriminant analysis (LDA) was proposed [8], with the objective of maximizing the between-class variance while minimizing the within-class variance by projecting the data into a lower-dimensional space. Nevertheless, LDA requires true class annotations and is hard to separate complex manifolds that cohere closely well using linear mapping.

High-dimensional data often exhibits a nonlinear manifold structure. It refers to the property where the intrinsic dimension of data is lower than the feature dimension, and the local topological structure is nearly Euclidean. To deal with data manifolds, manifold learning has emerged as a pioneering approach, surpassing traditional dimension reduction methods. The concept of manifold learning was first derived from isometric feature mapping (Isomap) [9] and locally linear embedding (LLE) [10]. Isomap exploits the shortest path distances measured in the K-nearest neighbors (KNN) graph [11], while LLE recovers manifold structure based on the locally linear relationships of data in high-dimensional space. Subsequently, a series of related methods, e.g., Laplacian eigenmaps [12], Hessian eigenmaps [13], and diffusion maps [14] were proposed successively. These methods focus on the preservation of the manifold structure, but ignore the discrimination of clusters, thereby making clusters overlapped in lower-dimensional space. As a revolutionary innovation, t-distributed stochastic neighbor embedding (t-SNE) [15] has received widespread attention in machine learning and data science since its inception. By utilizing two different probability distributions, t-SNE can better preserve distinct gaps between the clusters. The success of t-SNE has also inspired a bunch of manifold learning methods such as parametric t-SNE [16], Barnes-Hut-SNE [17], viSNE [18], LargeVis [19], uniform manifold approximation and projection (UMAP) [20], opt-SNE [21], self-organizing nebulous growths (SONG) [22] and so on. Among these techniques, UMAP has been extensively applied in many fields [23]. It assumes that the local neighborhoods lie on a Riemannian manifold, and improves the initialization, cost function, and optimizer of t-SNE. Consequently, it can achieve higher separation of clusters and more efficient computation compared to t-SNE. Whereas, UMAP still suffers from computational problems for data with large sizes and high dimensions, and is insufficient to preserve the global structure only through Laplacian eigenmaps initialization [24].

The time-efficiency issue of t-SNE-based manifold learning has received attention, and the improvement mainly forms three research directions: utilizing high-performance computing (HPC), optimizing the learning process with the Barnes-Hut algorithm, and landmark sampling approaches. HPC-based methods have requirements for computational hardware, and the algorithms must be reconstructed to adapt to the HPC framework [25, 26, 27]. BH-t-SNE algorithm accelerates gradient computation through the quadtree data structure, but it only enables 2-D or 3-D embedding due to the high time complexity for constructing the high-dimensional tree-based index [17]. In comparison, landmark sampling is a more immediate and valid measure to enhance efficiency by selecting a subset of data points as landmarks. The original research work of t-SNE [15] recommends a random landmark sampling strategy that has been achieved in [28]. However, the outcomes are unstable, especially when processing data with large heterogeneity in densities and cluster sizes. To construct the global skeleton, AtSNE chooses the cluster centroids generated by K-means as landmarks [29] and yields multiple times speed-up over BH-t-SNE on the GPU platform, but it also suffers from data heterogeneity. Therefore, for producing stable and faithful embedding, a robust landmark sampling strategy that is capable of overcoming data heterogeneity is highly

desired, as well as other components of manifold learning, namely preprocessing, initialization, optimization, non-landmark embedding, and so on.

In this work, we develop a scalable manifold learning method, namely scML. Its core idea aims to sample a subset of points as landmarks participated in manifold learning, and then incorporate the non-landmarks into the learned low-dimensional space. Our contributions can be summarized in three facets. Firstly, a novel landmark sampling strategy called plum pudding sampling (PPS) is proposed, enabling a quick and uniform landmark sampling through neighborhood exclusion. Secondly, the entire manifold learning framework is optimized. We perform early aggregation on the landmarks to modify the Gaussian-based high-dimensional probability and define a logarithmic low-dimensional probability. Laplacian eigenmaps is adopted for initialization, and the gradient descent is updated by a momentum method and adaptive learning rate. Thirdly, we design a constrained locally linear embedding (CLLE) subject to the nearest distance for incorporating the non-landmarks. Compared with the mainstream baselines, scML presents distinct advantages in scalability and time efficiency. With changes in sample rate, scML can maintain a high level of embedding quality while ensuring the stability of the global structure. The enhancement of time efficiency is derived from reducing the number of samples involved in manifold learning through PPS, and achieving a faster convergence for embedding optimization than the Student-t distribution through the logarithmic low-dimensional probability. The robustness of scML is credited to PPS, early aggregation, and CLLE. The landmarks generated by PPS are uniformly distributed throughout the data, and fully capture the global skeleton. Early aggregation and CLLE suppress the dirty clusters caused by oversampling, which ensures inter-cluster separation and cluster integrity simultaneously. In terms of the global structure, landmark sampling expands the neighborhood of the points involved in manifold learning in a sense, thereby representing the topological structure at longer distances. Besides, Laplacian eigenmaps is capable of yielding an initial layout with a better global structure.

## Results

### Overview of scML

The high time consumption of t-SNE primarily arises from the computation of a large matrix over hundreds of epochs during the learning stage. Selecting a subset of key points as landmarks to participate in manifold learning can significantly improve time efficiency and scalability. We hence propose scML that consists of three major stages, sampling, learning, and incorporating, as illustrated in Fig. 1a. In the first stage, PPS is performed to choose the landmarks from the original data. These landmarks are then fed into the learning stage to obtain the landmark embedding by gradient descent. Subsequently, CLLE is employed to incorporate the non-landmarks into the learned lower-dimensional space and generate the ultimate embedding.

The challenge in sampling lies in how to maintain the structural similarity between the landmarks and the original data. Hence, plum pudding sampling (PPS) is proposed, which gets its name from the fact that the resulting landmarks have an approximately uniform distribution, resembling “plums” embedded in the original data “pudding”. Its workflow is illustrated in Fig. 1b and has been summarized as Algorithm 1 in Supplementary Note 1. Considering that the high-density points are more important, this approach arranges all points in descending order of their reversed nearest

neighbors (RNN) in advance. In each loop, we select the first point in the sorted point queue as a landmark and move its KNN from the queue to the non-landmark set. The loop continues until there are no points left in the queue. The sample rate is determined by the number of nearest neighbors  $k_1$ , with a larger number leading to a lower sample rate.

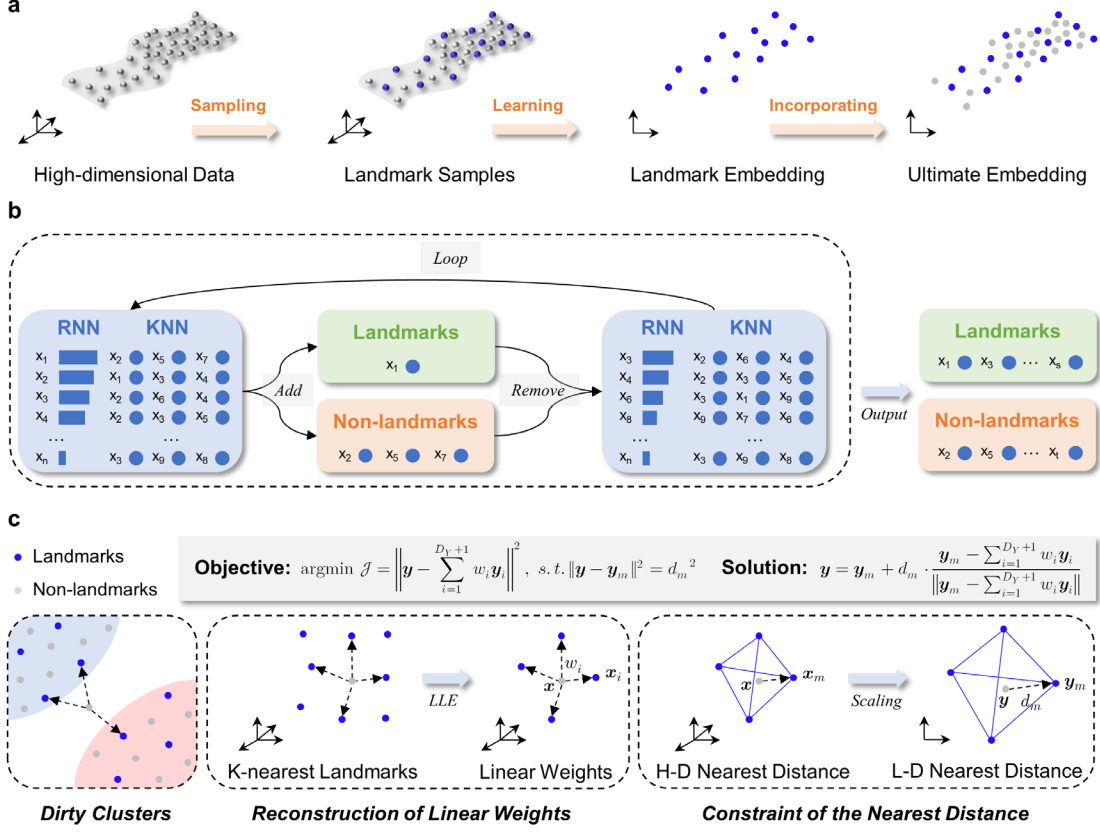


**Fig. 1. Illustration diagram of scML.** **a**, The overall framework of scML includes three main stages: (i) sampling landmarks from the original high-dimensional data; (ii) manifold learning to generate the lower-dimensional embedding of landmarks; (iii) obtaining the ultimate layout by incorporating non-landmarks to the lower-dimensional space. **b**, The workflow of PPS. The sorted points by their RNN are added to the landmark set in turn. Each time the first point in the queue is added, its KNN are then moved from the queue to the non-landmark set. We repeat this operation until there are no points left in the queue. **c**, Essentials of CLLE. The first row presents the objective and solution of CLLE, while the second row illustrates the dirty clusters and two components of CLLE, including the reconstruction of linear weights and calculation of the (L-D) nearest distance. Dirty clusters are generated by incorporating non-landmarks into the inter-cluster blanks only using locally linear relationships.

In the learning stage, we adopt the framework used by t-SNE, LargeVis, and UMAP to approximate the distribution between the high-dimensional probability  $P$  and low-dimensional probability  $Q$ , and optimize its core components for adapting to the sampling strategy and improving the efficiency of gradient descent. Oversampling may lose the agglomeration of clusters in the original data, making the sparse landmarks hard to be clustered accurately. To tackle the oversampling problem, we early aggragate the landmarks based on their original associations. The association degree between landmarks is measured by a shared nearest neighbor (SNN) metric. We then use a Gaussian

kernel to compute the high-dimensional conditional probability  $p_{j|i} = \exp(-d_{ji}^2/2\sigma_i^2)$ , where  $d_{ji}$  denotes the distance modified by early aggregation and  $\sigma_i$  refers to the variance of Gaussian. In t-SNE, LargeVis, and UMAP,  $\sigma_i$  is determined by performing a binary search on a specified perplexity; while we define it as the average KNN distances of  $x_i$ , to produce a uniform-density embedding and evade complex solving process. After performing Laplacian eigenmaps to generate an initial layout, we compute the low-dimensional probability  $q_{ij}$  between point  $\mathbf{y}_i$  and point  $\mathbf{y}_j$  with a logarithmic function

$$q_{ij} = \frac{(1 + \log(1 + \|\mathbf{y}_i - \mathbf{y}_j\|^2))^{-1}}{\sum_{k \neq i} (1 + \log(1 + \|\mathbf{y}_k - \mathbf{y}_i\|^2))^{-1}}$$

Logarithmic  $q_{ij}$  promotes a faster convergence for embedding optimization than the Student-t-based probability, and achieves stronger intra-cluster compactness. Kullback-Leibler divergence is leveraged as the cost function and can be minimized by the gradient descent method with a gradient of

$$\frac{\partial \mathcal{L}}{\partial \mathbf{y}_i} = 4 \sum_j \frac{(p_{ij} - q_{ij}) \cdot (\mathbf{y}_i - \mathbf{y}_j)}{(1 + \|\mathbf{y}_i - \mathbf{y}_j\|^2) \cdot (1 + \log(1 + \|\mathbf{y}_i - \mathbf{y}_j\|^2))}$$

We exploit a momentum method to speed up the gradient descent with an adaptive learning rate and momentum term. The learning rate is set using a constant warm-up strategy and cosine annealing schedule. The differences between t-SNE, UMAP, and scML can be seen in Supplementary Table 1, and more details about the preprocessing, initialization, optimization, and hyperparameter settings are in Methods.

The linear relationships with the nearest landmarks can be used to determine the proper position of the non-landmarks in the learned space. However, owing to the cluster proximity, the non-landmarks near the cluster boundaries tend to be inserted into the gaps between clusters, resulting in outliers and dirty clusters (Fig. 1c). We hence develop CLLE, which imposes a constraint of the nearest distance based on the naïve objective, besides utilizing LLE to reconstruct the linear weights with the nearest landmarks. The nearest distance constraint can effectively confine the non-landmarks within a small neighborhood estimated by scaling the high-dimensional nearest distance to their nearest landmarks. More details of CLLE can be found in Methods and Algorithm 6 in Supplementary Note 1.

### Validating the core components of scML on synthetic datasets

We assessed the core components and overall performance of scML by comparing with baselines and conducting ablation experiments on synthetic datasets. To evaluate the stability of landmark sampling by PPS, three sampling baselines including random sampling (RS), K-means sampling (KMS), and grid sampling (GS) were selected for the comparison on two 2-D synthetic datasets, DS1 [30] and DS2 [31], with clusters of different shapes and densities. For a fair comparison, these four methods were required to output the same number of landmarks. Since DS1 and DS2 contain different numbers of points, we set  $k_1$  for PPS from 2 to 20 on DS1 and 30 to 50 on DS2. In RS, sampling was carried out randomly based on the data index, while KMS and GS first partitioned the data into ten clusters and 4×4 regular grid cells respectively, and then performed random sampling

for each partition. The offset distance of centroids (ODOC) was used to evaluate the distribution consistency between the sampled landmarks and the original data. As shown in Fig. 2a, the landmarks produced by RS, KMS, and GS are randomly distributed and there exists many large blank regions, which introduces inescapable errors for preserving the structure of these regions. Meanwhile, the inherent randomness gives rise to unstable embedding results. In comparison, PPS generates more uniform landmarks, resulting in a much smaller ODOC even with a low sample rate, in turn beneficial for subsequent dimension reduction to maintain the global structure in a stable manner.

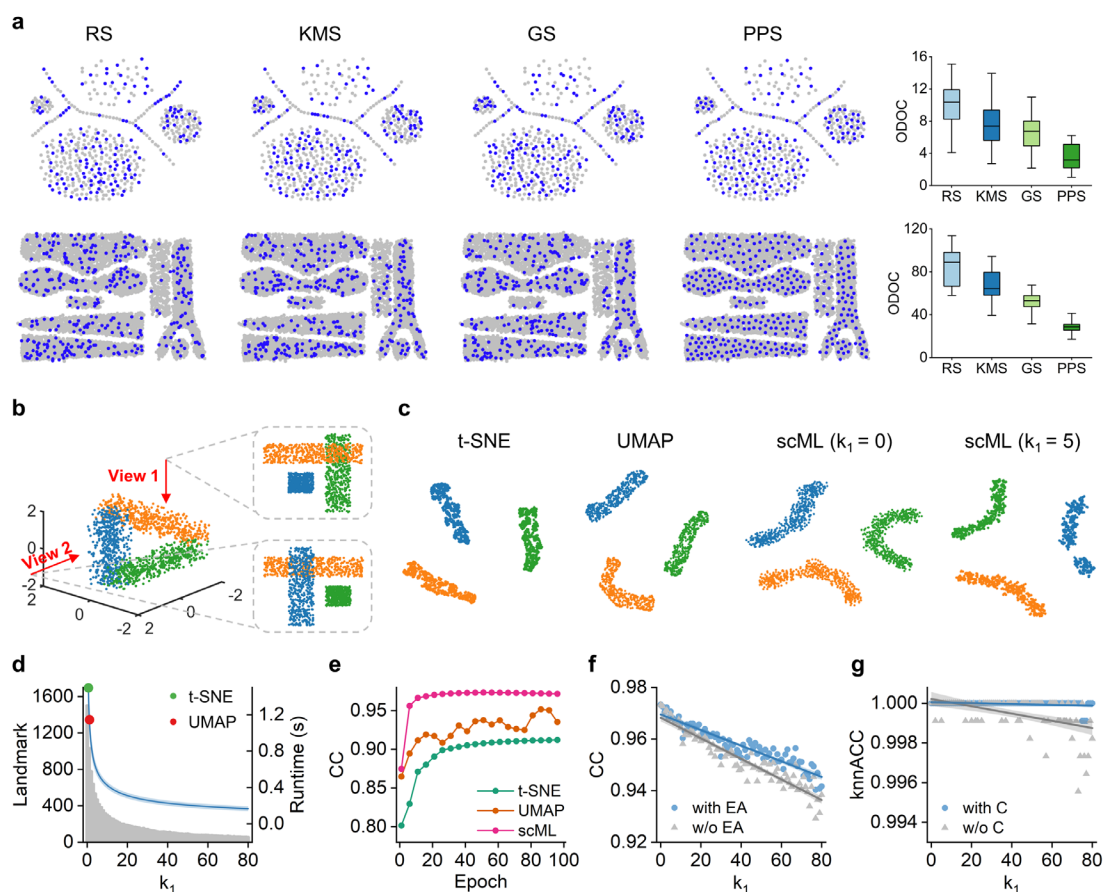


**Fig. 2. Performance on synthetic datasets.** **a**, The landmarks generated by RS, KMS, GS, and PPS from two 2-D synthetic datasets (DS1 and DS2) with 524 and 7,677 points respectively. The boxes show the median and 5-95% range of ODOC score. **b**, A 3-D synthetic dataset, DS3, contains three cuboids that are perpendicular and equidistant from each other with 1,600 points. **c**, 2-D embeddings of t-SNE, UMAP, and scML on DS3. **d**, The gray bars show the number of landmarks generated by PPS, and the blue line presents the trend of scML runtime by varying  $k_1$ , with a 95% confidence band. The green and red dots show the runtimes of t-SNE and UMAP respectively. **e**, The trends of the CC score by t-SNE, UMAP, and scML ( $k_1 = 0$ ) over the iteration time of gradient descent. **f**, The trends of the CC score by scML with (blue) and without (gray) early aggregation under different values of  $k_1$ , whereas the shading shows a 95% confidence level of the trends. **g**, The trends of the knnACC score by scML with (blue) and without a constraint (gray) in LLE as  $k_1$  increases, with shading denoting a 95% confidence interval.

Furthermore, the overall performance of scML was validated on a 3-D synthetic dataset, DS3,

consisting of three elongated cuboids of equal length and spacing (Fig. 2b). The embeddings are presented in Fig. 2c, where scML preserves the equidistance relationship better than t-SNE and UMAP using only 461 landmarks under  $k_1 = 5$ . In terms of time efficiency, scML outperforms t-SNE and UMAP when  $k_1 \geq 2$ . The number of landmarks and runtime decrease rapidly with the increase of  $k_1$ , corresponding to a lower sample rate (Fig. 2d). It demonstrates the significant improvement in computational performance achieved by utilizing PPS. We also explored the trend of embedding quality over the iteration time of gradient descent using the congruence coefficient (CC) metric [32]. It quantifies the preservation of the global or macroscopic structure. As shown in Fig. 2e, the CC score of UMAP fluctuates markedly as the epoch increases, while scML achieves higher and more stable embedding quality in a faster convergence, which benefits from the logarithmic low-dimensional probability. To evaluate the effectiveness of early aggregation and CLLE for addressing the oversampling problem, we tested the performances of scML without early aggregation (w/o EA) and a constraint (w/o C) in LLE on DS3 respectively. Compared to the scML w/o EA, the complete scML produces a higher CC score, which decreases more slowly as  $k_1$  grows (Fig. 2f). In addition, the trend of the accuracy of a supervised classifier KNN (knnACC) [19, 29] indicates that scML w/o C generates more dirty clusters with outliers than the complete scML, leading to lower cluster discrimination. This effect is particularly noticeable when  $k_1$  is large and the sample rate is low (Fig. 2g).

### Practical efficacy on real-world datasets

We examined the practical efficacy of scML by comparing with three typical baselines, BH-t-SNE, UMAP, and TriMap [24], on 12 real-world datasets, including eight UCI benchmarks (Wine, Dermatology, Breast-Cancer, Mfeat, Rice, Spambase, Dry-Bean, and Shuttle) [33], three image datasets (CIFAR10 [34], MNIST [35], and FMNIST [36]), and a text dataset of news articles (AG’s News) [37]. More details about the datasets can be found in Supplementary Table 2. We specified the default parameters suggested by BH-t-SNE, UMAP, and TriMap. For scML, we set  $k_1 = 20$  for the eight UCI datasets, and  $k_1 = 50$  for CIFAR10, MNIST, FMNIST, and AG’s News by considering the data size. We implemented scML, BH-t-SNE, and UMAP in MATLAB R2022a on a commodity desktop computer with an 8-core Intel i7 processor and 256 GB RAM, while utilizing the cloud version of TriMap at <http://www.omic.ai>.

The 2-D embeddings from Shuttle, CIFAR10, MNIST, FMNIST, and AG’s News are illustrated in Fig. 3. In general, scML yields remarkable cluster discrimination, better cluster integrity, and more accurate global structure. For Shuttle, BH-t-SNE, UMAP, and TriMap split the cluster of “Rad Flow” (blue) into multiple parts and destroy the clusters of “High” (red) and “Bypass” (purple) into sub-clusters far apart. While scML better preserves the proximity of the points in clusters of “High” (red) and “Bypass” (purple), thereby protecting the cluster integrity. In terms of CIFAR10, scML pulls apart each cluster and generates less overlaying. It keeps the relative global relationship, for instance, the cluster of “automobile” (orange) is embedded close to the cluster of “truck” (cyan) due to the high similarity, but they are very separate in the layout of BH-t-SNE. BH-t-SNE also fails to preserve the global structure of MNIST, and breaks up the cluster of digit “1”. TriMap generates an overlarge layout of digit “1”. Such heterogeneity in cluster size is not conducive to data visualization, clustering, and classification. scML presents a similar map to UMAP, but separates digit “8” from the clump composed of digits “3” and “5”. This case also occurs in digit “7” and the clump of digits “4” and “9”. The fashion items in FMNIST are quite similar, resulting in most categories being mixed

and indistinguishable. Compared with the three competitors, scML not only pushes the categories of “Trouser” (orange) and “Bag” (olive) away from other categories, but also generates a distinct gap between two clumps, one containing classes of “T-shirt” (blue) and “Dress” (red), and the other having categories of “Pullover” (green), “Coat” (purple) and “Shirt” (pink). In AG’s News, BH-t-SNE completely damages the global structure, while scML generates a more distinguishable layout, and separates the clusters of “Business” (green) and “Science/Technique” (red) that are adjoined in the layouts of UMAP and TriMap.

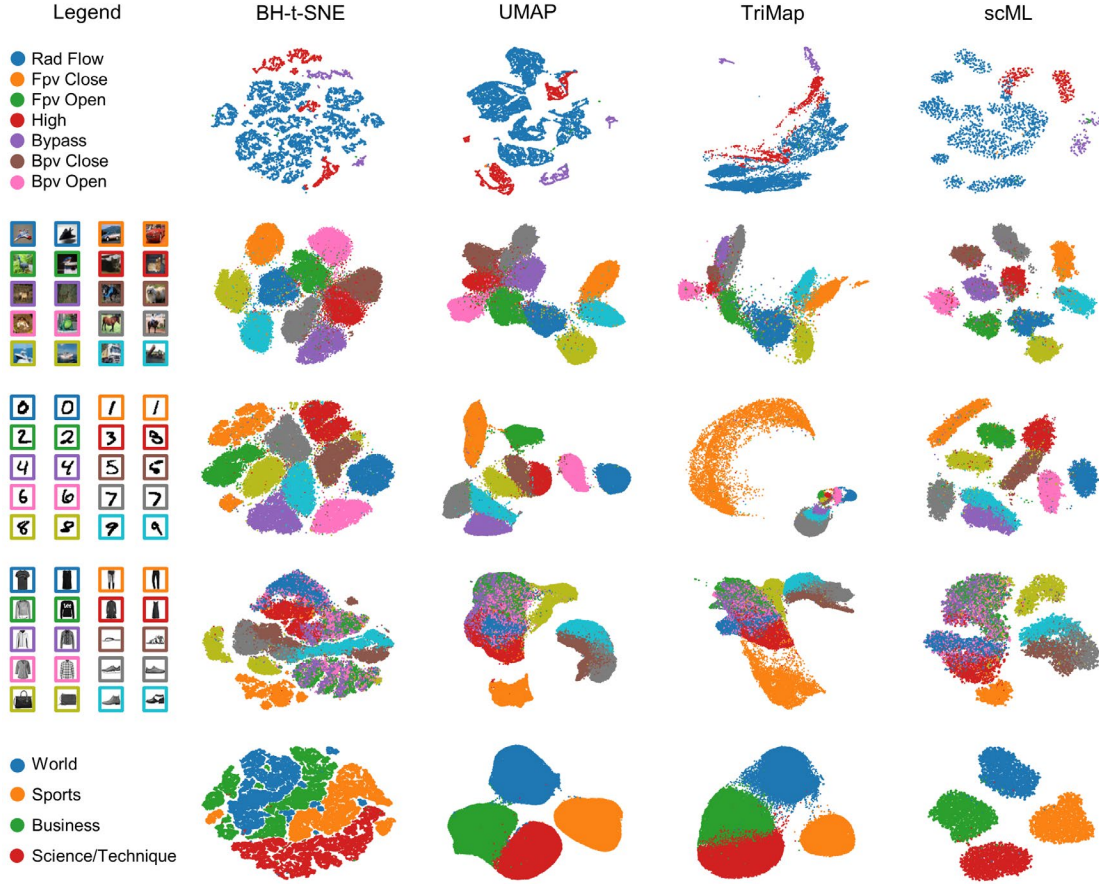


**Fig. 3. 2-D embeddings of BH-t-SNE, UMAP, TriMap, and scML from five real-world datasets, Shuttle, CIFAR10, MNIST, FMNIST, and AG’s News.**

We utilized the accuracy of KNN (knnACC), SVM (svmACC) [38] classifiers, and K-means clustering (clusACC) to evaluate the embedding quality quantitatively. As the results illustrated in Fig. 4a and Supplementary Table 3, scML obtains the highest score of knnACC, svmACC, and clusACC on eight, nine, and eleven datasets respectively, and outperforms by a large margin on Wine, Dermatology, Breast-Cancer, and Dry-Bean. As the relative runtimes shown in Fig. 4b, scML exhibits a significant advantage in time efficiency, ranking at the forefront on most datasets. Meanwhile, we evaluated the performance of scML by varying  $k_1$  from 0 to 200 on MNIST. The layout of the embedding is stable, and the clusters are separated well in Fig. 4c. Thus, the three metrics lie in a high score interval steadily in Fig. 4d. We also compared the proposed logarithmic low-dimensional probability  $q_{scml}$  with that of t-SNE and UMAP,  $q_{tsne}$  and  $q_{umap}$ , by integrating them with our method under the same configurations. By default, UMAP sets  $a = 1.93$  and  $b = 0.79$ . The formulas of the three probability functions and 2-D embeddings are illustrated

in Supplementary Fig. 1, and the clusACC scores are shown in Fig. 4e. It can be found that  $q_{scml}$  enhances the convergence speed of the embedding optimization compared to  $q_{tsne}$  and  $q_{umap}$ , and yields a promising layout within 30 epochs. For further testifying to the scalability, we benchmarked BH-t-SNE, UMAP, TriMap, and scML on the sub-samples of the full Yahoo dataset with 1.4 million samples. The result in Fig. 4f indicates that scML has superior scaling performance with data size, and only costs around 32 minutes on the full samples (6.5-fold faster than BH-t-SNE). Moreover, we validated the scaling performance with respect to the embedding dimension on Mfeat. Since BH-t-SNE and TriMap only support embedding high-dimensional data into 2- or 3-D space, we selected the exact t-SNE algorithm and UMAP for comparison. The result in Fig. 4g reveals that scML scales significantly better than t-SNE and UMAP as the embedding dimension increases.

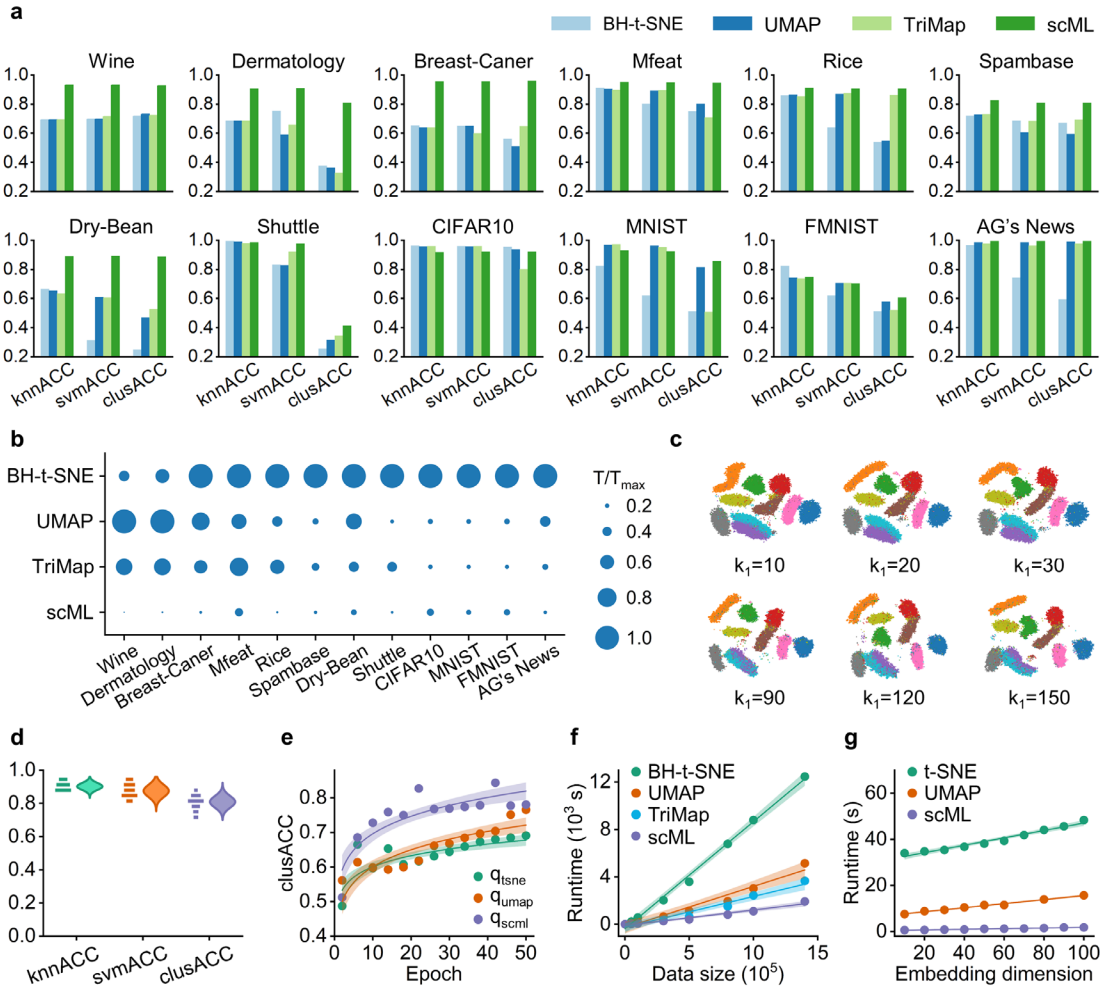


**Fig. 4. Quantitative comparison of the embedding quality and time efficiency on 13 real-world datasets.** **a**, knnACC, svmACC, and clusACC scores and **b**, relative runtimes of BH-t-SNE, UMAP, TriMap and scML on eight UCI benchmarks, three image datasets, and a text dataset of news articles, where the relative runtime denotes the absolute runtime divided by the maximum runtime on each dataset. **c**, 2-D embeddings, and **d**, the distributions of knnACC, svmACC and clusACC scores by scML as  $k_1$  varies from 0 to 200 on MNIST. **e**, Clustering accuracies of scML equipped with three low-dimensional probabilities under different epochs on MNIST, where the shading denotes a 95% confidence interval. **f**, Runtimes scaling on various sized sub-samples of the full Yahoo dataset with a 95% confidence band. BH-t-SNE, UMAP, and TriMap are equipped with the default parameters,

and  $k_1$  of scML is specified as  $\frac{n}{1000}$ , where  $n$  denotes the total number of points. **g**, Runtimes of t-SNE, UMAP, and scML under different embedding dimensions on Mfeat. The shading represents a 95% confidence interval.

## Application on the single-cell transcriptomics

In life science, exploring the spatial characteristic of single-cell transcriptomics is essential for unraveling the spatial organization and interactions of cells within tissues and organs, revealing the developmental processes and disease mechanisms, and identifying novel therapeutic targets [39, 40]. Dimension reduction provides critical insights into the spatial heterogeneity of cellular architecture, and helps to annotate different cell types within complex tissues and organs [41, 42]. To evaluate the applicability of our method, we applied scML to the single-cell RNA sequencing (scRNA-seq) and mass cytometry (CyTOF) data, and compared it with UMAP in terms of both embedding quality and time efficiency.

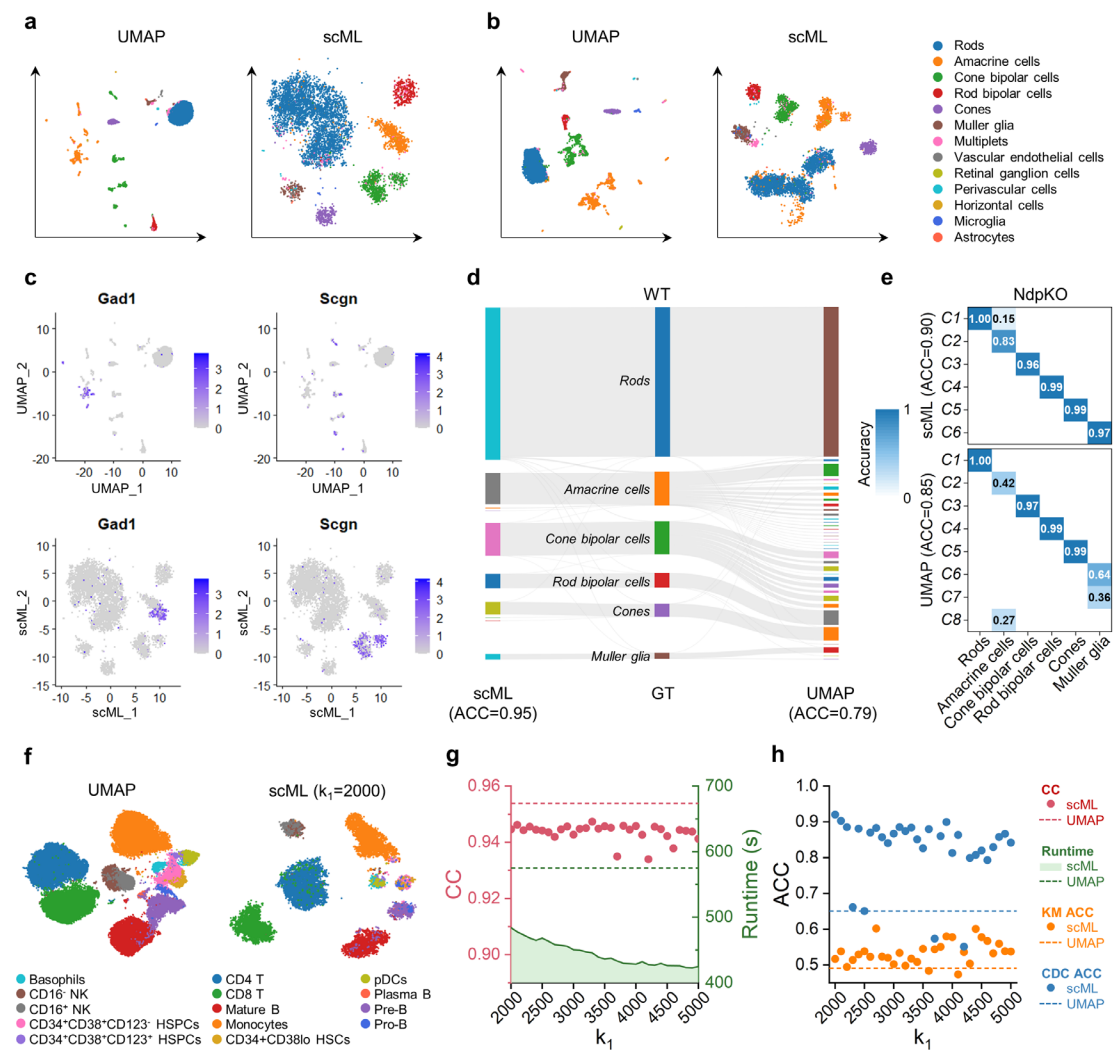


**Fig. 5. Performance on scRNA-seq and CyTOF data. a, b**, 2-D embeddings of UMAP and scML ( $k_1 = 20$ ) from two mouse retina scRNA-seq datasets, WT and NdpKO. **c**, Expression patterns of two differentially marker genes for amacrine and cone bipolar cells of WT retinas in the UMAP and scML plots. **d**, A Sankey diagram shows the match between the clustering results of CDC on the

embeddings and six reported cell type annotations (ground truth, GT) of WT retinas. **e**, A heatmap presents the identification accuracy of six cell types in NdpKO retinas using CDC algorithm. **f**, 2-D embeddings of UMAP and scML on the CyTOF dataset Levine. **g**, CC scores and runtimes of UMAP and scML by varying  $k_1$  from 2,000 to 5,000 on Levine. **h**, ACC scores of K-means (KM) and CDC algorithms on the UMAP and scML embeddings with different  $k_1$  on Levine.

The analysis was performed on two published scRNA-seq datasets from wild-type (WT) and Norrin-knockout (NdpKO) mouse retinas [43], which cover 7,695 and 7,640 cells with 27,998 genes respectively. We utilized the standard pipeline for scRNA-seq clustering to preprocess the two datasets, including quality control, normalization, selecting highly variable genes (HVG), scaling, and PCA [44]. The 2-D embeddings of UMAP and scML (Fig. 5a, b) were generated based on the 50-D PCA results. Compared to UMAP, scML generates embeddings with better preservation of the cluster integrity, particularly for amacrine and cone bipolar cells in WT. Fig. 5c and Supplementary Fig. 4 illustrate the spatial expression patterns of differentially marker genes (*Cnga1*, *Gad1*, *Scgn*, *Sebox*, *Opn1mw*, and *Gpr37*) corresponding to six major cell types (rods, amacrine cells, cone bipolar cells, rod bipolar cells, cones, Muller glia) in WT retinas. The cells with high expression levels of *Gad1* and *Scgn* in the scML plot exhibit a more concentrated distribution than the UMAP space. Accounting for the heterogeneity in cluster size and density, we performed a cutting-edge clustering algorithm, clustering by direction centrality (CDC) [45], with default parameters ( $k = 20$ ,  $ratio = 0.95$ ), on the 2-D embeddings to evaluate the discrimination between different cell types. As shown in the Sankey (Fig. 5d) and heatmap plots (Fig. 5e), the predicted results based on the scML embeddings stay more closely aligned with the true cell type annotations.

Moreover, we investigated the performance of scML on a CyTOF dataset Levine [46], containing 265,627 bone marrow cells with 32 protein markers and 14 populations. We followed the standard data preprocessing in Weber et al. 2016 [47]. scML pushes different cell types away from each other and generates more distinct gaps, especially between CD4 T cells and CD8 T cells, mature B cells, and pre-B cells (Fig. 5f). We measured the preservation of pairwise distances by CC metric. Under different  $k_1$ , the CC scores of scML are stable and high (Fig. 5g). Most of them stay in a narrow range of 0.94 to 0.95 and are slightly lower than the CC of UMAP (0.9539), but scML ran faster than UMAP (Fig. 5g). We also conducted an unsupervised clustering analysis using two algorithms, K-means and CDC, based on the 2-D embeddings. Most ACC scores upon the scML embeddings are higher. Especially in CDC results, scML leads UMAP by a large margin (Fig. 5h).

### **Application for detecting the abnormal heartbeats in ECG signals**

The electrocardiogram (ECG) is a non-invasive diagnostic technique used to assess the electrical activities of the heart [48]. It records the electrical signals during each heartbeat, providing valuable information about cardiac function, rhythm, and conduction system [49]. Cardiac anomalies can be reflected in the abnormal waveforms of an ECG signal. Detecting the anomalies contributes to the prompt diagnosis and management of cardiac diseases, ultimately improving patient outcomes [50]. To automatically detect abnormal heartbeats in ECG signals, we design an end-to-end workflow in Fig. 6a. Specifically, the Fourier synchrosqueezed transform (FSST) [51] is used to obtain time-frequency representations of the sample points in the signal. These representations are then fed into a pre-trained deep recurrent neural network to identify the P/QRS/T waves (Fig. 6b). Subsequently, we split the entire signal into beat-wise segments using the beginning points of the QRS complex

as breakpoints. Each ECG beat corresponds to a cardiac cycle, and comprises of a P wave, a QRS complex, and a T wave. From each beat segment, we extract eight waveform features, including four amplitude and four interval features (Fig. 6c). We apply three dimension reduction techniques, PCA, UMAP, and scML, to embed the features into a lower-dimensional space, and exploit KNN and SVM classifiers to distinguish the normal and abnormal heartbeats.

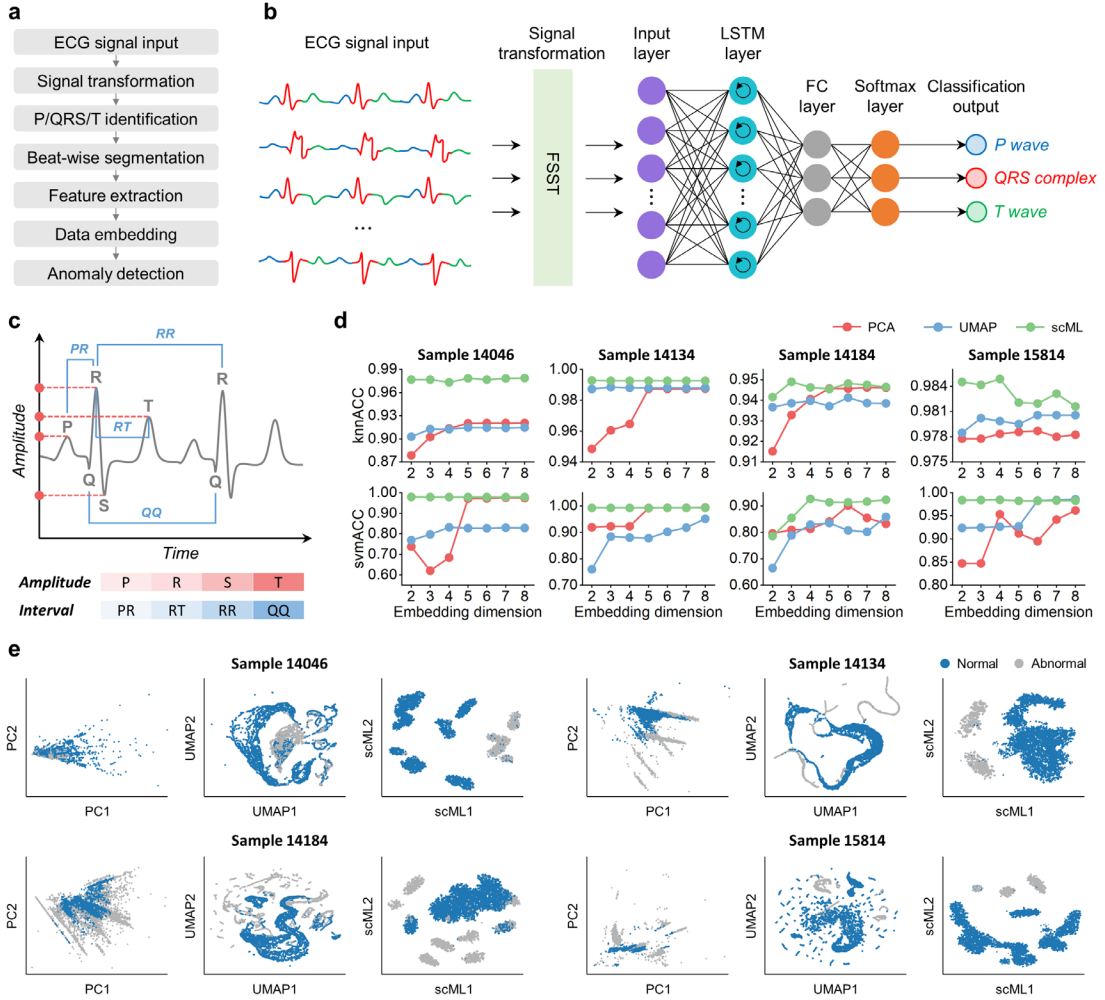


**Fig. 6. Recognition of the abnormal heartbeats in ECG signals.** **a**, The overall workflow to detect abnormal heartbeats. **b**, The deep neural network architecture used for identifying three types of waves in the training phase, composed of an input layer, an LSTM recurrent layer with 200 hidden units, a fully connected layer, a softmax layer, and a classification output layer. **c**, Schematic of eight waveform features, including four peak amplitudes of P, R, S, and T waves, and four interval features, PR, RT, RR and QQ intervals. **d**, ACC scores of KNN and SVM classifiers with different embedding dimensions by PCA, UMAP, and scML ( $k_1 = 20$ ). **e**, 2-D embeddings of PCA, UMAP, and scML on four ECG datasets.

Identifying the P/QRS/T waves is the fundamental step in the overall workflow. Considering the powerful capability of the long short-term memory (LSTM) network in learning and representing chronological sequences [52], an LSTM-based deep learning architecture was constructed for this purpose. The training phase of this architecture is depicted in Fig. 6b. We pre-trained this model using the published available QT database, which contains 210 fifteen-minute two-lead ECG

recordings from 105 patients. These recordings include the annotations of P, QRS, and T waves [53]. Each ECG signal consists of 225,000 sample points with a sample rate of 250 Hz. We randomly selected 70% of the signals as the training set and used the remaining as the test set. The FSST of the first 10,000 sample points in each signal were fed to the model. We used the Adam optimizer and set the mini-batch size, maximum number of epochs, initial learning rate, and gradient threshold to 2,000, 10, 0.01 and 1 respectively. This model finally yielded a training accuracy of 94.73% and a prediction accuracy of 95.59%.

To testify to the effectiveness of this workflow and the performance of scML, we chose four ECG recordings (sample 14046, 14134, 14184, and 15814) with a sample rate of 128 Hz from the MIT-BIH long-term database, which were collected from four cardiac patients of different ages [54]. Each sample point in the ECG signals has been manually annotated into five types, namely normal beat, premature ventricular contraction, fusion of ventricular and normal beat, junctional premature beat, and supraventricular premature beat. The four beat types, excluding the normal beat, were considered as anomalies. For each ECG recording, we intercepted signals from the first two and a half hours with 1,152,000 sample points and inputted them to the workflow. After calculating the waveform features of each beat segment, we conducted KNN and SVM classifiers on the embedded data obtained by the three dimension reduction methods. The ACC scores under different embedding dimensions are presented in Fig. 6d. In general, scML outperforms PCA and UMAP both in knnACC and svmACC on all four ECG datasets. Notably, scML exhibits greater stability as the embedding dimension varies. This indicates that scML can avoid crowded clusters even in low-dimensional spaces. The 2-D embeddings generated by PCA, UMAP and scML are displayed in Fig. 6e. In the PCA embeddings, normal and abnormal beats are mixed, making them hard to be separated. While UMAP produces too many tiny clusters that disrupt the global topological structure, especially on the samples 14184 and 15184. In contrast, scML excels in preserving the cluster integrity and inter-cluster distinction.

## Discussion

The goal of manifold learning is to stretch the underlying structure and generate a simpler and more concise representation in a lower-dimensional space. Real-world data generally comes from a bunch of variable spaces and exists in high ambient dimensions, concealing within intrinsic manifolds of lower dimensions. Such a manifold structure is not conducive to classification and clustering tasks, and imposes burdens on data storage and computation. Hence, a number of manifold learning algorithms have been developed, such as Isomap, LLE, t-SNE, and UMAP. However, they pay more attention to the local relationship but sometimes fail to preserve the global structure. Meanwhile, they are computationally expensive when dealing with large-scale and high-dimensional data. In this work, our proposed manifold learning method, namely scML, exhibits powerful scalability on various benchmarks and two application scenarios. The landmark sampling strategy PPS facilitates scML to preserve the global structure in a stable manner under different sample rates. PPS not only reduces the number of points involved in gradient calculations but also expands the neighborhood for capturing the topological structure at a longer distance. Introducing Laplacian eigenmaps for initialization also contributes to preserving the global structure and cluster integrity (Supplementary Fig. 2). Meanwhile, logarithmic low-dimensional probability function speedups the convergence of embedding optimization and can generate a separable layout in fewer epochs (Supplementary Fig.

1). To address the oversampling problem caused by low sample rate, SNN-based early aggregation is utilized to make the landmarks in the same cluster more compact, while CLLE ties the non-landmarks near their nearest landmarks, thereby avoiding the occurrence of dirty clusters.

scML has demonstrated significant potential and advantages in visualization and classification missions. Nonetheless, there remains limitations and room for further improvement. Like other manifold learning methods, scML is also less interpretable compared to the linear approaches such as PCA and LDA. The original physical meaning of the feature space will be lost when transformed into a latent space. Same as t-SNE and UMAP, scML tends to create an embedding with uniform point density and smooths out the original density differences. The number of landmarks generated by PPS decreases as  $k_1$  increases, and lies between  $n/k_1$  and  $n$ . Due to data heterogeneity, the exact number is hard to determine by  $k_1$ , which makes it tough to accurately estimate the time complexity. Hence, the accurate relation between  $k_1$  and the sample rate should be investigated. Meanwhile, scML adopts exact KNN search at present, which is time-consuming when handling large data size and high dimensionality, even with PCA preprocessing the data. An alternative approach is approximate nearest neighbor (ANN) that can be integrated with scML to enhance the time performance. Furthermore, the hyperparameter settings can be refined. Apart from  $k_1$ , the hyperparameters have either been fixed or adaptively specified based on empirical attempts. For example, scML fixes the aggregation coefficient  $\gamma = 1.2$  in early aggregation, but the most appropriate  $\gamma$  probably changes with the sample rate (Supplementary Fig. 3). Therefore, it would be beneficial to investigate better hyperparameter settings and combination strategies.

## Methods

### Preprocessing

After inputting the vector-based data, we first remove the duplicate observations and utilize min-max normalizing to standardize the scale of each feature into  $[0, 1]$ . Then, we conduct KNN search accordingly. scML involves two rounds of KNN search. The first round is dedicated to landmark sampling with  $k_1$  nearest neighbors, while the second is for constructing the high-dimensional probabilities of landmarks with  $k_2$  nearest neighbors. K-D tree can be used to accelerate this process when the data dimensionality is not high, but when handling excessive dimensions, the construction of the K-D tree becomes time-consuming. Thus, for data with more than 5,000 points (denoted as  $n > 5,000$ ) and 50 dimensions (denoted as  $D_X > 50$ ), we employ PCA to project the data into a lower-dimensional space beforehand, whose dimensionality is selected to ensure that the cumulative contribution rate is slightly above 0.8. To be noted, we only use PCA for the two rounds of KNN search, while manipulating the data of original dimensionality in other steps.

### Early aggregation

When clusters are close and the sample rate is low, the oversampling problem may occur. This problem causes the landmarks to be widely spread out, subsequently weakening their connections, and destroying the cluster discrimination. To tackle this problem, we consider that the landmarks with a significant number of SNN in the original data should maintain a high level of similarity in the sampled data. Additionally, SNN with a high local density (RNN) should carry more weight. Hence, we define the pairwise SNN as

$$SNN_{ij} = \sum_{\mathbf{x}_u \in KNN(\mathbf{x}_i) \cap KNN(\mathbf{x}_j)} RNN_u \quad (1)$$

where  $KNN(\mathbf{x}_i)$  refers to the KNN set of landmark  $\mathbf{x}_i \in \mathbb{R}^{D_x}$  with  $k_2$  nearest neighbors, and  $RNN_u$  denotes the RNN of point  $\mathbf{x}_u$ . Then, the distance of  $\mathbf{x}_j$  to  $\mathbf{x}_i$  can be modified as

$$d_{j|i} = \left( 1 - \frac{SNN_{ij}}{\max_i SNN_{ij}} \right)^\gamma \|\mathbf{x}_i - \mathbf{x}_j\| \quad (2)$$

where  $\gamma$  is the aggregation coefficient.

### High- and low-dimensional probabilities

When constructing the high-dimensional probabilities (Algorithm 2 in Supplementary Note 1), we only focus on the  $k_2$  nearest landmarks obtained by the modified distances in equation (2), while disregarding the points that are far away. Based on early aggregation, we employ a Gaussian kernel to calculate the conditional probabilities of landmark  $\mathbf{x}_j$  to landmark  $\mathbf{x}_i$

$$p_{j|i} = \begin{cases} \exp\left(-\frac{d_{j|i}^2}{2\sigma_i^2}\right), & \mathbf{x}_j \in KNN(\mathbf{x}_i) \\ 0, & else \end{cases} \quad (3)$$

The variance  $\sigma_i$  of Gaussian contributes to producing uniform densities of points in the embedding. In densely populated regions, it is more appropriate to use a smaller  $\sigma_i$ . Both t-SNE and UMAP find the optimal  $\sigma_i$  through a fixed perplexity and binary search. For improving the efficiency without sacrificing validity, we define  $\sigma_i$  as the average KNN distance of landmark  $\mathbf{x}_i$

$$\sigma_i = \frac{1}{k_2} \sum_{\mathbf{x}_j \in KNN(\mathbf{x}_i)} d_{j|i} \quad (4)$$

Subsequently, the high-dimensional probabilities can be normalized and symmetrized as

$$p_{ij} = \frac{p_{i|j} + p_{j|i}}{2 \sum_{k \neq l} p_{k|l}} \quad (5)$$

We adopt a logarithmic function to measure the low-dimensional probabilities

$$q_{ij} = \frac{(1 + \log(1 + \|\mathbf{y}_i - \mathbf{y}_j\|^2))^{-1}}{\sum_{k \neq l} (1 + \log(1 + \|\mathbf{y}_k - \mathbf{y}_l\|^2))^{-1}} \quad (6)$$

where the logarithmic  $q_{ij}$  makes the embedding optimization converge faster than the Student-t-based probability.

### Gradient descent

Kullback-Leibler divergence (KLD) is leveraged as the cost function

$$\mathcal{L} = \sum_{i \neq j} p_{ij} \log \frac{p_{ij}}{q_{ij}} \quad (7)$$

We can derive the gradient as

$$\frac{\partial \mathcal{L}}{\partial \mathbf{y}_i} = 4 \sum_j \frac{(p_{ij} - q_{ij})(\mathbf{y}_i - \mathbf{y}_j)}{(1 + \|\mathbf{y}_i - \mathbf{y}_j\|^2) (1 + \log(1 + \|\mathbf{y}_i - \mathbf{y}_j\|^2))} \quad (8)$$

The detailed derivation can be seen in Supplementary Note 2. By using gradient descent method with a momentum term, the update is given by

$$\mathbf{y}_i^{(t)} = \mathbf{y}_i^{(t-1)} - \eta(t) \left( \frac{\partial \mathcal{L}}{\partial \mathbf{y}_i^{(t)}} + \alpha(t) \frac{\partial \mathcal{L}}{\partial \mathbf{y}_i^{(t-1)}} \right) \quad (9)$$

where  $\mathbf{y}_i^{(t)} \in \mathbb{R}^{D_Y}$ ,  $\eta(t)$  and  $\alpha(t)$  are the low-dimensional coordinate of landmark  $\mathbf{x}_i$ , learning rate and momentum term in the  $t$ th epoch respectively.  $\mathbf{y}_i^{(0)}$  is initialized by Laplacian eigenmaps (Algorithm 3 in Supplementary Note 1), and the ultimate low-dimensional coordinates of landmarks can be obtained using Algorithm 4 in Supplementary Note 1.

### Constrained locally linear embedding

After obtaining the low-dimensional coordinates of landmarks, we proceed to incorporate the non-landmarks into the learned space. LLE can be exploited to fast embed non-landmarks using the locally linear relationship with  $D_Y + 1$  nearest landmarks, where  $D_Y$  represents the number of embedding dimensions. However, a non-landmark in the boundary areas tends to be mistakenly inserted into the inter-cluster gaps, since its nearest landmarks may belong to different clusters and be distantly located from each other, especially when  $k_1$  is large. This can result in dirty clusters with outliers. In order to evade this issue, we impose a constraint of the nearest distance on the naïve objective function of LLE

$$\operatorname{argmin} \mathcal{J} = \left\| \mathbf{y} - \sum_{i=1}^{D_Y+1} w_i \mathbf{y}_i \right\|^2, \quad s. t. \|\mathbf{y} - \mathbf{y}_m\|^2 = d_m^2 \quad (10)$$

where  $\mathbf{y} \in \mathbb{R}^{D_Y}$  represents the embedding coordinate of the current non-landmark  $\mathbf{x} \in \mathbb{R}^{D_x}$ ,  $\mathbf{y}_i$  and  $w_i$  denote the embedding coordinate and reconstructed linear weight of the  $i$ th nearest landmarks respectively.  $\mathbf{y}_m$  is the embedding coordinate of the nearest landmark to  $\mathbf{x}$ , and  $d_m$  is the low-dimensional distance between  $\mathbf{y}$  and  $\mathbf{y}_m$ .

Using Lagrange multiplier technique, we can derive the solution of  $\mathbf{y}$

$$\mathbf{y} = \mathbf{y}_m + d_m \frac{\mathbf{y}_m - \sum_{i=1}^{D_Y+1} w_i \mathbf{y}_i}{\left\| \mathbf{y}_m - \sum_{i=1}^{D_Y+1} w_i \mathbf{y}_i \right\|} \quad (11)$$

The entire flow of CLLC can be seen in Algorithm 6 in Supplementary Note 1, and the detailed derivation can be found in Supplementary Note 3.

The key to solve  $\mathbf{y}$  is to obtain  $w_i$  and  $d_m$ . Suppose that  $\mathbf{W} = [w_1, w_2, \dots, w_{D_Y+1}]^T \in \mathbb{R}^{D_Y+1}$  denotes the reconstructed linear weights of the current non-landmark  $\mathbf{x}$ , and let the matrix  $\mathbf{X} = [\mathbf{x}_1, \mathbf{x}_2, \dots, \mathbf{x}_{D_Y+1}] \in \mathbb{R}^{D_x \times (D_Y+1)}$  includes its  $D_Y + 1$  nearest landmarks, then we can restate the object of LLE as

$$\operatorname{argmin} \phi = \mathbf{W}^T \mathbf{G} \mathbf{W}, s. t. \mathbf{1}^T \mathbf{W} = 1 \quad (12)$$

where  $\mathbf{G} = (\mathbf{x}\mathbf{1}^T - \mathbf{X})^T(\mathbf{x}\mathbf{1}^T - \mathbf{X}) \in \mathbb{R}^{(D_Y+1) \times (D_Y+1)}$  and  $\mathbf{1} = [1, 1, \dots, 1]^T \in \mathbb{R}^{D_Y+1}$ . It is worth noting that sometimes the Gram matrix  $\mathbf{G}$  is singular or nearly singular, in which case it should be replaced by  $\mathbf{G} + \left(\frac{\Delta^2}{D_Y+1}\right) \cdot \operatorname{tr}(\mathbf{G}) \cdot \mathbf{I}$  [55, 56], where  $\Delta = 0.1$  and  $\mathbf{I} \in \mathbb{R}^{(D_Y+1) \times (D_Y+1)}$  is the identity matrix, thus we can obtain the solution

$$\mathbf{W} = \frac{\mathbf{G}^{-1}\mathbf{1}}{\mathbf{1}^T \mathbf{G}^{-1}\mathbf{1}} \quad (13)$$

To compute  $d_m$ , we first calculate the high-dimensional distance between  $\mathbf{x}$  and  $\mathbf{x}_m$ , then transform it by the optimal distance scale. The optimal scale of  $\mathbf{y}_m$  can be solved by seeking the mapping relationship between the high- and low-dimensional distances between the KNN of  $\mathbf{y}_m$

$$\operatorname{argmin} C = \sum_{i=1}^{\frac{k_2(k_2-1)}{2}} (\text{scale} \cdot d_i - d'_i)^2 \quad (14)$$

where  $d_i$  and  $d'_i$  denote the  $i$ th pairwise distances between the KNN of  $\mathbf{y}_m$  in high- and low-dimensional spaces respectively. Set the derivative of  $C$  to 0

$$\frac{\partial C}{\partial \text{scale}} = 2 \sum_{i=1}^{\frac{k_2(k_2-1)}{2}} d_i (\text{scale} \cdot d_i - d'_i) = 0 \quad (15)$$

Then, we can solve the optimal scale

$$\text{scale} = \frac{\sum_{i=1}^{\frac{k_2(k_2-1)}{2}} d_i d'_i}{\sum_{i=1}^{\frac{k_2(k_2-1)}{2}} d_i^2} \quad (16)$$

Hence, we can obtain  $d_m$

$$d_m = \|\mathbf{y} - \mathbf{y}_m\| = \text{scale} \cdot \|\mathbf{x} - \mathbf{x}_m\| \quad (17)$$

The detailed procedure to compute the optimal scale has been summarized as Algorithm 5 in Supplementary Note 1.

## Hyperparameter settings

In the first-round KNN search, the parameter  $k_1$  controls the sample rate and affects the time efficiency of scML. Users have the flexibility to specify it according to their requirements by trading off the efficiency and quality. For  $k_2$  in the second-round KNN search, since the parameter of KNN is typically associated with the number of landmarks  $N$  [57], we hence provide an empirical strategy to determine it

$$k_2 = \begin{cases} \lceil \log_2 N \rceil + 18, N \geq 1,000 \\ \left\lceil \frac{N}{50} \right\rceil + 8, 50 \leq N \leq 1,000 \\ 9, 9 \leq N \leq 50 \\ N, N < 9 \end{cases} \quad (18)$$

where  $\lceil \cdot \rceil$  denotes the nearest integer upwards. In the learning stage, we fix the aggregation coefficient to  $\gamma = 1.2$  for SNN-based early aggregation. We adaptively adjust the learning rate using a constant warm-up strategy and cosine annealing schedule [58]

$$\eta(t) = \begin{cases} \eta_{max}, & t \leq T_{warm} \\ \eta_{min} + \left(\frac{\eta_{max} - \eta_{min}}{2}\right) \left(1 + \cos\left(\frac{t - T_{warm}}{t - T_{epoch}}\pi\right)\right), & else \end{cases} \quad (19)$$

where the maximum and minimum learning rates are set to  $\eta_{max} = 2.5N$  and  $\eta_{min} = 2N$ , the number of warm-up epochs and training epochs are specified to  $T_{warm} = 10$  and  $T_{epoch} = 50$  respectively. Besides, the momentum term can be adaptively set to  $\alpha(t) = \frac{t-1}{t+2}$  in the  $t$ th epoch.

## Evaluation metrics

### Offset distance of centroids

The offset distance of centroids (ODOC) is used to quantify the distribution consistency between the data before and after sampling, which is formulated as

$$ODOC = \sum_{i=1}^c \|C_i - C'_i\|^2 \quad (20)$$

where  $c$  refers to the number of clusters,  $C_i$  and  $C'_i$  denote the centroid of the  $i$ th cluster before and after sampling.

### Congruence coefficient

The congruence coefficient (CC) is able to evaluate the preservation of the global or macroscopic structure in embedding. It is defined as the cosine similarity between pairwise distances in the high-dimensional space and in the embedding

$$CC = \frac{\sum_{i=1}^{\frac{n(n-1)}{2}} d_i \cdot d'_i}{\sqrt{\sum_{i=1}^{\frac{n(n-1)}{2}} d_i^2} \cdot \sqrt{\sum_{i=1}^{\frac{n(n-1)}{2}} d_i'^2}} \quad (21)$$

where  $d_i$  and  $d'_i$  denote the  $i$ th corresponding pairwise distances in high- and low-dimensional spaces respectively.

### Accuracy of KNN, SVM classifiers, and K-means clustering

To measure the separation of clusters in the lower-dimensional space, we leverage the accuracy (ACC) of two supervised classifiers, i.e., KNN and support vector machine, and a clustering algorithm, K-means. KNN and SVM classifiers involve the following steps: (a) apply a nonlinear dimension reduction method to obtain the  $D_Y$ -dimensional embedding; (b) use 25% samples as the training set, and 75% samples as the test set to evaluate the performance of KNN and SVM classifiers. (c) compute the average ACC score from the five times of training. The  $k$  in KNN classifier is specified as 5. K-means is performed on the  $D_Y$ -dimensional embeddings with the true number of clusters and 200 iterations.

ACC refers to the accuracy rate of the classification or clustering results compared with the true labels. We set the true label vector and the predicted label vector as  $\mathbf{l} = (l_1, l_2, \dots, l_n) \in \mathbb{R}^n$  and  $\mathbf{r} = (r_1, r_2, \dots, r_n) \in \mathbb{R}^n$  respectively, and the ACC can be defined as:

$$\text{ACC} = \frac{\sum_{i=1}^n \delta(l_i, \text{map}(r_i))}{n} \quad (22)$$

where  $\delta(\cdot)$  denotes an indicator function:

$$\delta(a, b) = \begin{cases} 1 & \text{if } a = b \\ 0 & \text{otherwise} \end{cases} \quad (23)$$

$\text{map}(\cdot)$  is a mapping function that maps each predicted label to one of the true cluster labels. Commonly, the best mapping can be found by using the Kuhn-Munkres or Hungarian Algorithm.

## Data availability

The real-world datasets used in this study are publicly available: Wine (<http://archive.ics.uci.edu/dataset/109/wine>), Dermatology (<http://archive.ics.uci.edu/dataset/33/dermatology>), Breast-Cancer (<https://www.csie.ntu.edu.tw/~cjlin/libsvmtools/datasets/binary/breast-cancer>), Mfeat (<https://archive.ics.uci.edu/dataset/72/multiple+features>), Rice (<https://archive.ics.uci.edu/dataset/545/rice+cammeo+and+osmancik>), Spambase (<https://archive.ics.uci.edu/dataset/94/spambase>), Dry-Bean (<https://archive.ics.uci.edu/dataset/602/dry+bean+dataset>), Shuttle (<https://archive.ics.uci.edu/dataset/148/statlog+shuttle>), CIFAR10 (<https://www.cs.toronto.edu/~kriz/cifar.html>), MNIST (<https://yann.lecun.com/exdb/mnist/>), FMNIST (<https://github.com/zalandoresearch/fashion-mnist>), AG's News ([http://www.di.unipi.it/~gulli/AG\\_corpus\\_of\\_news\\_articles.html](http://www.di.unipi.it/~gulli/AG_corpus_of_news_articles.html)), Yahoo (<https://github.com/zjulearning/AtSNE>), WT, NdpKO (GSE125708), Levine (FlowRepository: FR-FCM-ZZPH), QT database (<https://www.mathworks.com/supportfiles/SPT/data/QTDatabaseECGData.zip>), MIT-BIH long term database (<https://archive.physionet.org/physiobank/database/ltadb/>).

## Code availability

The source code of scML in MATLAB and Python versions has been deposited at <https://github.com/ZPGuiGroupWhu/scml>.

## References

1. Waggoner, P. D. Modern dimension reduction. Preprint at <https://arxiv.org/abs/2103.06885> (2021).
2. Liang, S., Sun, Y. & Liang F. Nonlinear sufficient dimension reduction with a stochastic neural network. Preprint at <https://arxiv.org/abs/2210.04349> (2022).
3. Peng, D., Gui, Z. & Wu, H. Interpreting the curse of dimensionality from distance concentration and manifold effect. Preprint at <https://arxiv.org/abs/2401.00422> (2023).
4. Vogelstein, J. T., Bridgeford, E. W., Tang, M. et al. Supervised dimensionality reduction for big data. *Nat. Commun.* **12**, 2872 (2021).

5. Hotelling, H. Analysis of a complex of statistical variables into principal components. *J. Educ. Psychol.* **25**, 417-441 (1933).
6. Kruskal, J. B. Multidimensional scaling by optimizing goodness of fit to a nonmetric hypothesis. *Psychometrika* **29**, 1-27 (1964).
7. Peng, D., Gui, Z. & Wu, H. A robust and efficient boundary point detection method by measuring local direction dispersion. Preprint at <https://arxiv.org/abs/2312.04065> (2023).
8. Fisher, R. A. The use of multiple measurements in taxonomic problems. *Ann. Eugenics* **7**, 179-188 (1936).
9. Tenenbaum, J. B., Silva, V. D. & Langford, J. C. A global geometric framework for nonlinear dimensionality reduction. *Science* **290**, 2319-2323 (2000).
10. Roweis, S. T. & Saul, L. K. Nonlinear dimensionality reduction by locally linear embedding. *Science* **290**, 2323-2326 (2000).
11. Cover, T. & Hart, P. Nearest neighbor pattern classification. *IEEE Trans. Inf. Theory* **13**, 21-27 (1967).
12. Belkin, M. & Niyogi, P. Laplacian eigenmaps and spectral techniques for embedding and clustering. In *Advances in neural information processing systems*, pp. 585-591 (NeurIPS, 2002).
13. Donoho, D. L. & Grimes, C. Hessian eigenmaps: Locally linear embedding techniques for high-dimensional data. *Proc. Natl. Acad. Sci. U. S. A.* **100**, 5591-5596 (2003).
14. Coifman, R. R. et al. Geometric diffusions as a tool for harmonic analysis and structure definition of data: diffusion maps. *Proc. Natl. Acad. Sci. U. S. A.* **102**, 7426-7431 (2005).
15. van der Maaten, L. & Hinton, G. Visualizing data using t-SNE. *J. Mach. Learn. Res.* **9**, 2579-2605 (2008).
16. van der Maaten, L. Learning a parametric embedding by preserving local structure, In *Proceedings of Artificial Intelligence and Statistics*, vol. 5, pp. 384-391 (2009).
17. van der Maaten, L. Accelerating t-SNE using tree-based algorithms. *J. Mach. Learn. Res.* **15**, 3221-3245 (2014).
18. Amir, A. D. et al. viSNE enables visualization of high dimensional single-cell data and reveals phenotypic heterogeneity of leukemia. *Nat. Biotechnol.* **31**, 545-552 (2013).
19. Tang, J., Liu, J., Zhang, M. & Mei, Q. Visualizing large-scale and high-dimensional data. In *Proceedings of the 25th International World Wide Web Conference*, pp. 287-297 (2016).
20. McInnes, L., Healy, J., Saul, N. & Großberger, L. UMAP: uniform manifold approximation and projection. *J. Open Source Softw.* **3**, 861 (2018).
21. Belkina, A. C. et al. Automated optimized parameters for T-distributed stochastic neighbor embedding improve visualization and analysis of large datasets. *Nat. Commun.* **10**, 5415 (2019).
22. Senanayake, D. A., Wang, W., Naik, S. H. & Halgamuge, S. Self-organizing nebulous growths for robust and incremental data visualization. *IEEE Trans. Neural Netw. Learn. Syst.* **32**, 4588-4602 (2021).
23. Becht, E. et al. Dimensionality reduction for visualizing single-cell data using UMAP. *Nat. Biotechnol.* **37**, 38-44 (2019).
24. Amid, E. & Warmuth, M. K. TriMap: large-scale dimensionality reduction using triplets. Preprint at <https://arxiv.org/abs/1910.00204> (2022).
25. Chan, D. M., Rao, R., Huang, F. & Canny, J. F. t-SNE-CUDA: GPU-accelerated t-SNE and its applications to modern data. Preprint at <https://arxiv.org/abs/1807.11824> (2018).

26. Meyer, B. H., Pozo, A. T. R. & Zola, W. M. N. Global and local structure preserving GPU t-SNE methods for large-scale applications. *Expert Syst. Appl.* **201**, 116918 (2022).
27. Wang, Y. et al. Optimizing and accelerating space-time Ripley's K function based on Apache Spark for distributed spatiotemporal point pattern analysis. *Future Gener. Comput. Syst.* **105**, 96-118 (2020).
28. Kobak, D. & Berens, P. The art of using t-SNE for single-cell transcriptomics. *Nat. Commun.* **10**, 5416 (2019).
29. Fu, C., Zhang, Y., Cai, D. & Ren, X. AtSNE: efficient and robust visualization on GPU through hierarchical optimization. In *Proceedings of the 25th ACM SIGKDD International Conference on Knowledge Discovery & Data Mining*, pp. 176-186 (2019).
30. Peng, D., Gui, Z. & Wu, H. MeanCut: a greedy-optimized graph clustering via path-based similarity and degree descent criterion. Preprint at <https://arxiv.org/abs/2312.04067> (2023).
31. Karypis, G., Han, E.-H. & Kumar, V. Chameleon: hierarchical clustering using dynamic modeling. *Computer*, **32**, 68-75 (1999).
32. France, S. & Carroll, D. Development of an agreement metric based upon the Rand Index for the evaluation of dimensionality reduction techniques, with applications to mapping customer data. In *Machine Learning and Data Mining in Pattern Recognition* (eds Perner, P.) vol. 4571, pp. 499-517 (2007).
33. Dua, D. & Graff, C. UCI machine learning repository. University of California, School of Information and Computer Science, Irvine, CA, (2019).
34. Krizhevsky, A. & Hinton, G. Learning multiple layers of features from tiny images. Technical Report (Univ. Toronto, 2009).
35. Lecun, Y., Bottou, L., Bengio, Y. & Haffner, P. Gradient-based learning applied to document recognition. *Proceedings of the IEEE* **86**, 2278-2324 (1998).
36. Xiao, H., Rasul, K. & Vollgraf, R. Fashion-MNIST: a novel image dataset for benchmarking machine learning algorithms. Preprint at <https://arxiv.org/abs/1708.07747> (2017).
37. Corso, G. M. D., Gulli, A. & Romani, F. Ranking a stream of news. In *Proceedings of the 14th International World Wide Web Conference*, pp. 97-106 (2005).
38. Huang, H., Wang, Y., Rudin, C. & Browne, E. P. Towards a comprehensive evaluation of dimension reduction methods for transcriptomic data visualization. *Commun. Biol.* **5**, 719 (2022).
39. Pliner, H. A., Shendure, J. & Trapnell, C. Supervised classification enables rapid annotation of cell atlases. *Nat. Methods* **16**, 983-986 (2019).
40. Chen, X. et al. Cell type annotation of single-cell chromatin accessibility data via supervised Bayesian embedding. *Nat. Mach. Intell.* **4**, 116-126 (2022).
41. Adil, A., Kumar, V., Jan A. T. & Asger, M. Single-cell transcriptomics: current methods and challenges in data acquisition and analysis. *Front. Neurosci.* **15**, 591122 (2021).
42. Qian, J., Liao, J., Liu, Z. et al. Reconstruction of the cell pseudo-space from single-cell RNA sequencing data with scSpace. *Nat. Commun.* **14**, 2484 (2023).
43. Heng J. S. et al. Hypoxia tolerance in the Norrin-deficient retina and the chronically hypoxic brain studied at single-cell resolution. *Proc. Natl. Acad. Sci. U. S. A.* **116**, 9103-9114 (2019).
44. Kiselev, V. Y., Andrews, T. S. & Hemberg, M. Challenges in unsupervised clustering of single-cell RNA-seq data. *Nat. Rev. Genet.* **20**, 273-282 (2019).

45. Peng, D. et al. Clustering by measuring local direction centrality for data with heterogeneous density and weak connectivity. *Nat. Commun.* **13**, 5455 (2022).
46. Levine, J. H. et al. Data-driven phenotypic dissection of AML reveals progenitor-like cells that correlate with prognosis. *Cell* **162**, 184-197 (2015).
47. Weber, L. M. & Robinson, M. D. Comparison of clustering methods for high-dimensional single-cell flow and mass cytometry data. *Cytom. Part A* **89**, 1084-1096 (2016).
48. Young, W. J. et al. Genetic analyses of the electrocardiographic QT interval and its components identify additional loci and pathways. *Nat. Commun.* **13**, 5144 (2022).
49. Niroshana, S. M. I., Kuroda, S., Tanaka, K. & Chen, W. Beat-wise segmentation of electrocardiogram using adaptive windowing and deep neural network. *Sci. Rep.* **13**, 11039 (2023).
50. Huo, R. et al. ECG segmentation algorithm based on bidirectional hidden semi-Markov model. *Comput. Biol. Med.* **150**, 106081 (2022).
51. Oberlin, T., Meignen, S. & Perrier, V. The fourier-based synchrosqueezing transform. In *IEEE International Conference on Acoustics, Speech and Signal Processing*, pp. 315-319 (ICASSP, 2014).
52. Hochreiter, S. & Schmidhuber, J. Long short-term memory. *Neural Comput.* **9**, 1735-1780 (1997).
53. Laguna, P., Mark, R. G., Goldberg, A. & Moody, G. B. A database for evaluation of algorithms for measurement of QT and other waveform intervals in the ECG. *Comput. Cardiol.* **24**, 673-676 (1997).
54. Goldberger, A. L. et al. PhysioBank, PhysioToolkit, and PhysioNet: components of a new research resource for complex physiologic signals. *Circulation* **101**, e215-e220 (2000).
55. Saul, L. K. & Roweis, S. T. Think globally, fit locally: unsupervised learning of low dimensional manifolds. *J. Mach. Learn. Res.* **4**, 119-155 (2003).
56. Wang, J. Real local-linearity preserving embedding. *Neurocomputing* **136**, 7-13 (2014).
57. Ding, J., Shah, S. & Condon, A. densityCut: an efficient and versatile topological approach for automatic clustering of biological data. *Bioinformatics* **32**, 2567-2576 (2016).
58. Loshchilov, I. & Hutter, F. SGDR: stochastic gradient descent with warm restarts. Preprint at <https://arxiv.org/abs/1608.03983> (2016).

## Supplementary Information

### Supplementary Note 1: Pseudocode of the algorithms

---

**Algorithm 1** Plum pudding sampling (PPS)

---

*Input:* Point set  $\mathbf{X}$  and the KNN parameter  $k_1$

- 1: Search the KNN and obtain the RNN of  $\mathbf{X}$  with  $k_1$
- 2: Arrange  $\mathbf{X}$  as  $\{\mathbf{x}_1, \mathbf{x}_2, \dots, \mathbf{x}_n\}$  in RNN descending order
- 3: Define an empty landmark set  $\mathbf{X}_l$  and non-landmark set  $\mathbf{X}_{nl}$
- 4: **for** the first point  $\mathbf{x}_i$  in  $\mathbf{X}$
- 5:     Add  $\mathbf{x}_i$  to  $\mathbf{X}_l$
- 6:     Move  $\mathbf{x}_a, \mathbf{x}_b, \dots, \mathbf{x}_s \in KNN(\mathbf{x}_i)$  from  $\mathbf{X}$  to  $\mathbf{X}_{nl}$
- 7: **end for**
- 8: **return**  $\mathbf{X}_l$  and  $\mathbf{X}_{nl}$

---

---

**Algorithm 2** Constructing the high-dimensional probabilities

---

*Input:* Landmark set  $\mathbf{X}_l$  and the KNN parameter  $k_2$

- 1: Search the KNN of  $\mathbf{X}_l$  with  $k_2$
- 2: Compute the pair-wise SNN using equation (1)
- 3: Compute the pair-wise distances of landmarks using equation (2)
- 4: **for** each point  $\mathbf{x}_i$  in  $\mathbf{X}_l$
- 5:     **for** each point  $\mathbf{x}_j$  in  $\mathbf{X}_l$
- 6:         **if**  $\mathbf{x}_j \in KNN(\mathbf{x}_i)$
- 7:              $p_{j|i} = \exp(-d_{j|i}^2 / 2\sigma_i^2)$  where  $\sigma_i$  can be obtained using equation (4)
- 8:         **else**
- 9:              $p_{j|i} = 0$
- 10:         **end if**
- 11:     **end for**
- 12: **end for**
- 13: Normalize and symmetrize the probability matrix as  $\mathbf{P}$  using equation (5)
- 14: **return**  $\mathbf{P}$

---

---

**Algorithm 3** Initialization using Laplacian eigenmaps

---

*Input:* High-dimensional probability matrix  $\mathbf{P}$  and embedding dimension  $D_Y$

- 1: Compute the degree matrix  $\mathbf{D}$
- 2: Compute the Laplacian matrix  $\mathbf{L} = \mathbf{D}^{1/2}(\mathbf{D} - \mathbf{P})\mathbf{D}^{1/2}$
- 3: Compute the eigenvectors  $[\mathbf{v}_1, \mathbf{v}_2, \dots, \mathbf{v}_N]$  of  $\mathbf{L}$  in ascending order of eigenvalues
- 4:  $\mathbf{Y}_l = [\mathbf{v}_2, \mathbf{v}_3, \dots, \mathbf{v}_{D_Y+1}]$
- 5: **return**  $\mathbf{Y}_l$

---

---

**Algorithm 4** Embedding optimization

---

*Input:* High-dimensional probability matrix  $P$ , initial landmark embedding  $Y_l$ , the maximum and minimum learning rates  $\eta_{max}$  and  $\eta_{min}$ , the number of warm-up epochs  $T_{warm}$  and training epochs  $T_{epoch}$

- 1: Compute the initial low-dimensional probability matrix  $Q$  using equation (6)
  - 2: **while**  $t < T_{epoch}$
  - 3:     Compute the learning rate using equation (19)
  - 4:     Compute the gradients using equation (8)
  - 5:     Update  $Y_l$  using equation (9)
  - 6:     Update  $Q$  using equation (6)
  - 7:      $t = t + 1$
  - 8: **end while**
  - 9: **return**  $Y_l$
- 

---

**Algorithm 5** Calculating the optimal scale

---

*Input:* KNN and embedding  $Y_l$  of the landmark set  $X_l$

- 1: **for** each point  $x_i$  in  $X_l$
  - 2:     Compute the pair-wise distances of  $KNN(x_i)$  using  $X_l$
  - 3:     Compute the pair-wise distances of  $KNN(x_i)$  using  $Y_l$
  - 4:     Compute the optimal scale  $scale_i$  of point  $x_i$  using equation (16)
  - 5: **end for**
  - 6: **return**  $scale = [scale_1, scale_2, \dots, scale_N]$
- 

---

**Algorithm 6** Constrained locally linear embedding

---

*Input:* Non-landmark set  $X_{nl}$ , embedding  $Y_l$  of the landmark set  $X_l$ , optimal scale  $scale$ , and embedding dimension  $D_Y$

- 1: **for** each point  $x_i$  in  $X_{nl}$
  - 2:     Search  $D_Y + 1$  nearest landmarks of  $x_i$  in  $X_l$
  - 3:     Compute the locally linear weights using equation (13)
  - 4:     Compute the nearest distance with  $scale_i$  using equation (17)
  - 5:     Compute the embedding  $y_i$  of  $x_i$  with  $Y_l$  using equation (11)
  - 6: **end for**
  - 7: Obtain the embedding  $Y_{nl} = [y_1, y_2, \dots, y_{n-N}]$  of  $X_{nl}$
  - 8: **return**  $Y_{nl}$
-

## Supplementary Note 2: Gradient of the KDL cost function

We leverage the Kullback-Leibler divergence (KLD) as the cost function

$$\mathcal{L} = KL(P||Q) = \sum_{i \neq j} p_{ij} \log \frac{p_{ij}}{q_{ij}} = \sum_{i \neq j} p_{ij} \log p_{ij} - p_{ij} \log q_{ij}$$

Let  $d_{ij} = \|\mathbf{y}_i - \mathbf{y}_j\|^2$ , then we have

$$\frac{\partial \mathcal{L}}{\partial \mathbf{y}_i} = -\frac{\partial(\sum_{k \neq l} p_{kl} \log q_{kl})}{\partial \mathbf{y}_i} = -2(\mathbf{y}_i - \mathbf{y}_j) \sum_j \frac{\partial(\sum_{k \neq l} p_{kl} \log q_{kl})}{\partial d_{ij}}$$

Let  $\Psi(\mathbf{y}_i, \mathbf{y}_j) = (1 + \log(1 + d_{ij}))^{-1}$ , we can obtain

$$\begin{aligned} \frac{\partial(\sum_{k \neq l} p_{kl} \log q_{kl})}{\partial d_{ij}} &= \sum_{k \neq l} p_{kl} \frac{\partial \log(\Psi(\mathbf{y}_k, \mathbf{y}_l)) - \partial \log(\sum_{k \neq l} \Psi(\mathbf{y}_k, \mathbf{y}_l))}{\partial d_{ij}} \\ &= \sum_{k \neq l} p_{kl} \frac{\partial \log(\Psi(\mathbf{y}_k, \mathbf{y}_l))}{\partial d_{ij}} - \left( \sum_{k \neq l} p_{kl} \right) \left( \frac{\partial \log(\sum_{k \neq l} \Psi(\mathbf{y}_k, \mathbf{y}_l))}{\partial d_{ij}} \right) \\ &= 2p_{ij} \frac{1}{\Psi(\mathbf{y}_i, \mathbf{y}_j)} \frac{\partial \Psi(\mathbf{y}_i, \mathbf{y}_j)}{\partial d_{ij}} - 2 \frac{1}{\sum_{k \neq l} \Psi(\mathbf{y}_k, \mathbf{y}_l)} \left( \frac{\partial \Psi(\mathbf{y}_i, \mathbf{y}_j)}{\partial d_{ij}} \right) \\ &= -2(p_{ij} - q_{ij}) \Psi(\mathbf{y}_i, \mathbf{y}_j) (1 + d_{ij})^{-1} \end{aligned}$$

Thus, we can derive the gradient as

$$\frac{\partial \mathcal{L}}{\partial \mathbf{y}_i} = 4 \sum_j \frac{(p_{ij} - q_{ij})(\mathbf{y}_i - \mathbf{y}_j)}{(1 + \|\mathbf{y}_i - \mathbf{y}_j\|^2) (1 + \log(1 + \|\mathbf{y}_i - \mathbf{y}_j\|^2))}$$

### Supplementary Note 3: Solving the constrained locally linear embedding

We modify the native objective function of LLE by imposing a constraint of the nearest distance

$$\operatorname{argmin} \mathcal{J} = \left\| \mathbf{y} - \sum_{i=1}^{D_Y+1} w_i \mathbf{y}_i \right\|^2, \quad s. t. \|\mathbf{y} - \mathbf{y}_m\|^2 = d_m^2$$

Using Lagrange multiplier technique, we introduce a new variable  $\lambda$  and define a new function as

$$\mathcal{J} = \left\| \mathbf{y} - \sum_{i=1}^{D_Y+1} w_i \mathbf{y}_i \right\|^2 - \lambda (\|\mathbf{y} - \mathbf{y}_m\|^2 - d_m^2)$$

We set the gradient of  $\mathcal{J}$  to a zero vector

$$\frac{\partial \mathcal{J}}{\partial \mathbf{y}} = 2 \left( \mathbf{y} - \sum_{i=1}^{D_Y+1} w_i \mathbf{y}_i \right) - 2\lambda (\mathbf{y} - \mathbf{y}_m) = \mathbf{0}$$

Then, we have

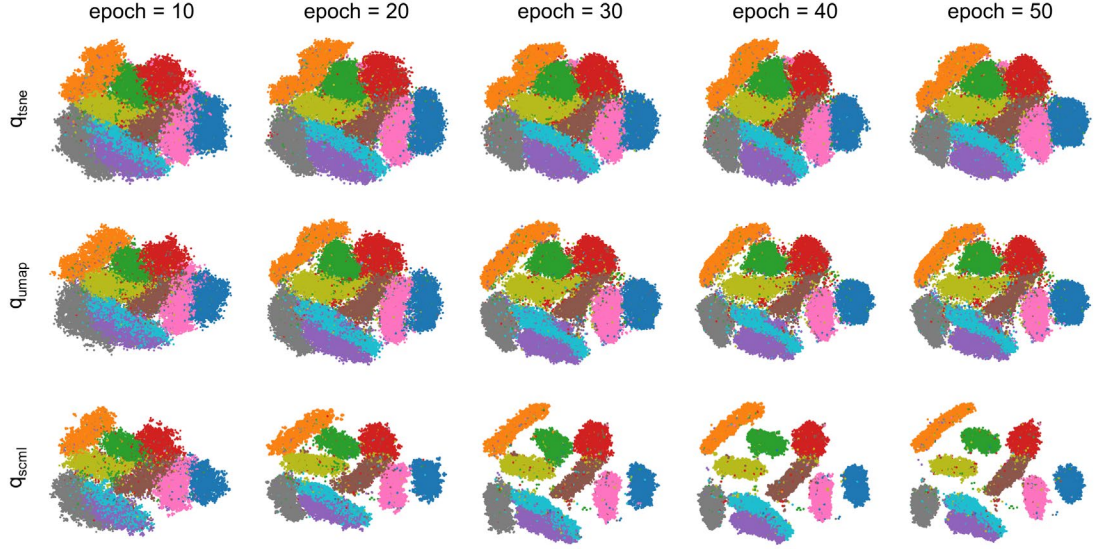
$$\mathbf{y} - \mathbf{y}_m = \frac{\mathbf{y}_m - \sum_{i=1}^{D_Y+1} w_i \mathbf{y}_i}{\lambda - 1}$$

Considering the constraint, we have

$$\|\mathbf{y} - \mathbf{y}_m\|^2 = \frac{\left\| \mathbf{y}_m - \sum_{i=1}^{D_Y+1} w_i \mathbf{y}_i \right\|^2}{(\lambda - 1)^2} = d_m^2$$

We can obtain the solution of  $\mathbf{y}$

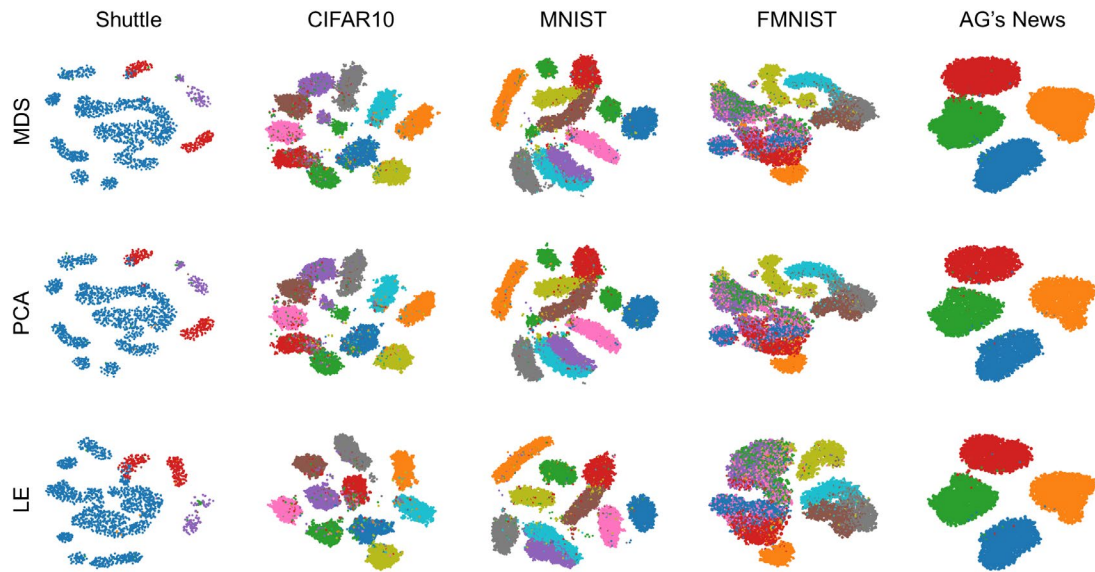
$$\mathbf{y} = \mathbf{y}_m + \frac{\mathbf{y}_m - \sum_{i=1}^{D_Y+1} w_i \mathbf{y}_i}{\lambda - 1} = \mathbf{y}_m + d_m \frac{\mathbf{y}_m - \sum_{i=1}^{D_Y+1} w_i \mathbf{y}_i}{\left\| \mathbf{y}_m - \sum_{i=1}^{D_Y+1} w_i \mathbf{y}_i \right\|_2}$$



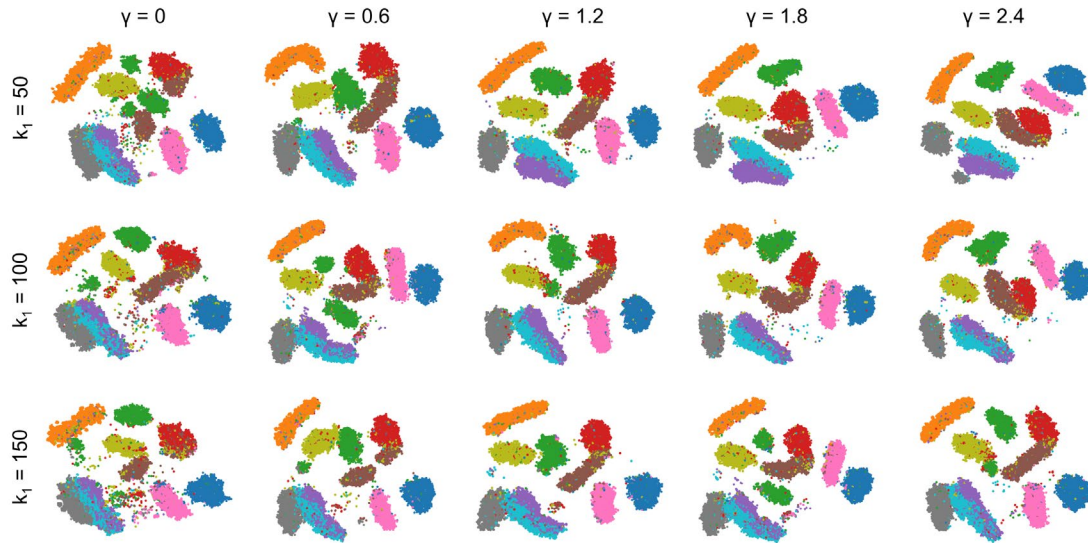
**Supplementary Fig. 1. 2-D embeddings of scML using three low-dimensional probability functions on MNIST.** We compared the low-dimensional probabilities of t-SNE, UMAP, and scML,

$$q_{tsne} = (1 + \|y_i - y_j\|^2)^{-1}, q_{umap} = (1 + a\|y_i - y_j\|^{2b})^{-1}, q_{scml} = (1 + \log(1 + \|y_i - y_j\|^2))^{-1},$$

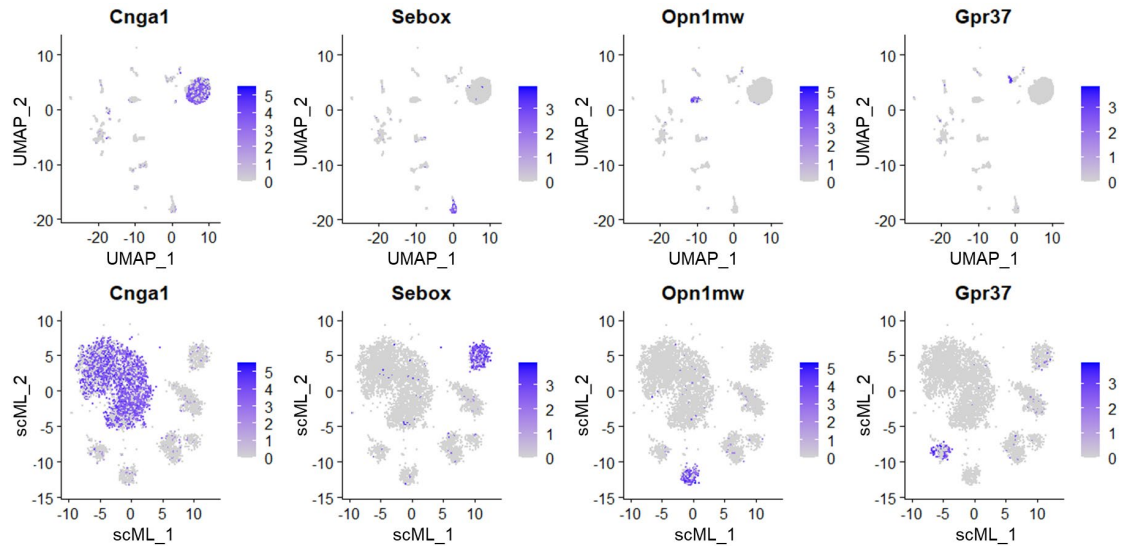
where the defaults in UMAP are set as  $a = 1.93$  and  $b = 0.79$ , and all other configurations are the same. The results show the effectiveness of the logarithmic low-dimensional probability.  $q_{scml}$  can accelerate the convergence speed of embedding optimization compared to  $q_{tsne}$  and  $q_{umap}$ , and yield a promising layout within 30 epochs.



**Supplementary Fig. 2. 2-D embeddings of scML using three initialization methods on five real-world datasets.** We employed three initialization methods in the learning stage of scML. In general, the outcomes of all these three methods are promising, but Laplacian eigenmaps (LE) slightly outperforms MDS and PCA. LE better aggregated together the points of “High” (red) in Shuttle, “bird” (green) in CIFAR10, digit “2” (green) in MNIST, and “Bag” (olive) in FMNIST.



**Supplementary Fig. 3. 2-D embeddings of scML by varying  $k_1$  and  $\gamma$  on MNIST.** The results show the effectiveness of SNN-based graph aggregation. scML without SNN ( $\gamma = 0$ ) splits the digit “2” (green) into multiple pieces, while scML with SNN better preserves the cluster integrity, and produces fewer outliers in the inter-cluster gaps. Furthermore, we can see that the optimal aggregation coefficient  $\gamma$  varies as  $k_1$ . For example, when the sample rate is large ( $k_1 = 100$ ), the embedding quality is optimal with  $\gamma = 1.8$  or  $\gamma = 2.4$ .



**Supplementary Fig. 4.** Expression patterns of differentially marker genes, Cnga1, Sebox, Opn1mw, and Gpr37 for rods, rod bipolar cells, cones, and Muller glia of WT retinas in the UMAP and scML plots.

**Supplementary Table 1: Differences between t-SNE, UMAP and scML in the learning stage.**

	<b>t-SNE</b>	<b>UMAP</b>	<b>scML</b>
Distance (take Euclidean distance for example)	$d_{ij} = \ \mathbf{x}_i - \mathbf{x}_j\ $	$d_{ij} = \ \mathbf{x}_i - \mathbf{x}_j\ $	$d_{ji} = \left(1 - \frac{SNN_{ij}}{\max_i SNN_{ij}}\right)^\gamma \ \mathbf{x}_i - \mathbf{x}_j\ $
High-dimensional conditional probabilities	$p_{ji} = \exp\left(-\frac{d_{ij}^2}{2\sigma_i^2}\right)$	$p_{ji} = \exp\left(-\frac{d_{ij} - \rho_i}{\sigma_i}\right)$	$p_{ji} = \exp\left(-\frac{d_{ji}^2}{2\sigma_i^2}\right)$
Gaussian bandwidth	$Prep = 2^{-\sum_j p_{ji} \log p_{ji}}$	$\sum_{\mathbf{x}_j \in KNN(\mathbf{x}_i)} \exp\left(-\frac{d_{ij} - \rho_i}{\sigma_i}\right) = \log_2 k$	$\sigma_i = \frac{1}{k} \sum_{\mathbf{x}_j \in KNN(\mathbf{x}_i)} d_{ji}$
Normalization and symmetrization	$p_{ij} = \frac{p_{ij} + p_{ji}}{2n \sum_{k \neq l} p_{k l}}$	$p_{ij} = p_{ji} + p_{i j} - p_{ji} p_{i j}$	$p_{ij} = \frac{p_{ij} + p_{ji}}{2 \sum_{k \neq l} p_{k l}}$
Low-dimensional conditional probabilities	$q_{ij} = \frac{(1 + \ \mathbf{y}_i - \mathbf{y}_j\ ^2)^{-1}}{\sum_{k \neq l} (1 + \ \mathbf{y}_k - \mathbf{y}_l\ ^2)^{-1}}$	$q_{ij} = (1 + a\ \mathbf{y}_i - \mathbf{y}_j\ ^{2b})^{-1}$	$q_{ij} = \frac{(1 + \log(1 + \ \mathbf{y}_i - \mathbf{y}_j\ ^2))^{-1}}{\sum_{k \neq l} (1 + \log(1 + \ \mathbf{y}_k - \mathbf{y}_l\ ^2))^{-1}}$
Cost function	$\mathcal{L} = \sum_{i \neq j} p_{ij} \log \frac{p_{ij}}{q_{ij}}$	$\mathcal{L} = \sum_{i \neq j} p_{ij} \log \frac{p_{ij}}{q_{ij}} + (1 - p_{ij}) \log \left(\frac{1 - p_{ij}}{1 - q_{ij}}\right)$	$\mathcal{L} = \sum_{i \neq j} p_{ij} \log \frac{p_{ij}}{q_{ij}}$
Initialization	<i>Random initialization</i>	<i>Laplacian eigenmaps</i>	<i>Laplacian eigenmaps</i>
Optimizer	$\mathbf{y}_i^{(t)} = \mathbf{y}_i^{(t-1)} - \eta \frac{\partial \mathcal{L}}{\partial \mathbf{y}_i^{(t)}} - \alpha(t)(\mathbf{y}_i^{(t-1)} - \mathbf{y}_i^{(t-2)})$	<i>Stochastic gradient descent and negative sampling</i>	$\mathbf{y}_i^{(t)} = \mathbf{y}_i^{(t-1)} - \eta(t) \left( \frac{\partial \mathcal{L}}{\partial \mathbf{y}_i^{(t)}} + \alpha(t) \frac{\partial \mathcal{L}}{\partial \mathbf{y}_i^{(t-1)}} \right)$

**Supplementary Table 2: Information of the 13 real-world datasets.**

Dataset	Description	# of Samples	Dimensions	Classes
Wine	UCI	178	13	3
Dermatology	UCI	358	34	6
Breast-Cancer	UCI	683	10	2
Mfeat	UCI	2,000	649	10
Rice	UCI	3,810	7	2
Spambase	UCI	4,601	57	2
Dry-Bean	UCI	13,611	16	7
Shuttle	UCI	14,500	9	7
CIFAR10	Color Images	60,000	1,024	10
MNIST	Handwritten Digits	70,000	784	10
FMNIST	Fashion Products	70,000	784	10
AG's News	Text Documents	120,000	100	4
Yahoo	Text Documents	1,400,000	100	10

**Wine, Dermatology, Breast-Cancer, Mfeat, Rice, Spambase, Dry-Bean, and Shuttle** are eight UCI datasets, in which features denote some attributes of real-world instances.

**CIFAR10** is a dataset including 60,000  $32 \times 32$  color images in 10 classes, with 6,000 images per class. Each image has been applied to a convolutional neural network to generate 1024-D features.

**MNIST** contains 70,000 grayscale images of handwritten digits from 0 to 9 with the size of  $28 \times 28$ . We convert the 2-D images to 1-D vectors and input into the process of dimension reduction.

**FMNIST** consists of 70,000  $28 \times 28$  pixel grayscale images and includes ten categories of fashion products (T-shirt, trouser, pullover, dress, coat, sandal, shirt, sneaker, bag, and ankle boot). Like with MNIST, FMNIST is also treated as 70,000 different 784-D vectors.

**AG's News** collects news articles in four categories (world, sports, business, and science technique). Each article is represented by a 100-D vector generated by FastText [1].

**Yahoo** has 1,400,000 news articles, which have been applied to FastText to extract 100-D features.

## Reference

[1] Joulin, A., Grave, E., Bojanowski, P. & Mikolov, T. Bag of tricks for efficient text classification. Preprint at <https://arxiv.org/abs/1607.01759> (2016).

**Supplementary Table 3: Evaluation metrics of BH-t-SNE, UMAP, TriMap and scML on 12 real-world datasets.**

		knnACC	svmACC	clusACC	Runtime (s)
Wine	BH-t-SNE	0.6917	0.6993	0.7191	0.44
	UMAP	0.6917	0.6993	0.7303	0.99
	TriMap	0.6917	0.7143	0.7247	0.68
	scML	<b>0.9323</b>	<b>0.9323</b>	<b>0.9270</b>	<b>0.02</b> ( $k_1=20$ )
Dermatology	BH-t-SNE	0.6866	0.7537	0.3771	0.66
	UMAP	0.6866	0.5933	0.3631	1.14
	TriMap	0.6866	0.6605	0.3268	0.80
	scML	<b>0.9067</b>	<b>0.9104</b>	<b>0.8101</b>	<b>0.03</b> ( $k_1=20$ )
Breast-Cancer	BH-t-SNE	0.6523	0.6504	0.5622	1.98
	UMAP	0.6406	0.6504	0.5125	1.47
	TriMap	0.6406	0.5996	0.6471	1.10
	scML	<b>0.957</b>	<b>0.9570</b>	<b>0.9590</b>	<b>0.07</b> ( $k_1=20$ )
Mfeat	BH-t-SNE	0.9127	0.8020	0.7515	2.87
	UMAP	0.9040	0.8927	0.8005	1.81
	TriMap	0.9000	0.8973	0.7090	2.20
	scML	<b>0.9527</b>	<b>0.9487</b>	<b>0.9450</b>	<b>0.62</b> ( $k_1=20$ )
Rice	BH-t-SNE	0.8600	0.6391	0.5399	5.79
	UMAP	0.8642	0.8715	0.5488	2.47
	TriMap	0.8533	0.8778	0.8633	3.44
	scML	<b>0.9135</b>	<b>0.9062</b>	<b>0.9071</b>	<b>0.26</b> ( $k_1=20$ )
Spambase	BH-t-SNE	0.7203	0.6870	0.6716	11.53
	UMAP	0.7293	0.6061	0.5964	2.98
	TriMap	0.7319	0.6835	0.6922	3.72
	scML	<b>0.8270</b>	<b>0.8101</b>	<b>0.8085</b>	<b>1.35</b> ( $k_1=20$ )
Dry-Bean	BH-t-SNE	0.6641	0.3147	0.2499	23.86
	UMAP	0.6534	0.6094	0.4685	15.80
	TriMap	0.6338	0.6077	0.5273	10.11
	scML	<b>0.8899</b>	<b>0.8941</b>	<b>0.8867</b>	<b>5.87</b> ( $k_1=20$ )
Shuttle	BH-t-SNE	<b>0.9925</b>	0.8315	0.2555	29.13
	UMAP	0.9918	0.8298	0.3161	4.80
	TriMap	0.9812	0.9218	0.3429	12.00
	scML	0.9860	<b>0.9783</b>	<b>0.4146</b>	<b>2.67</b> ( $k_1=20$ )
CIFAR10	BH-t-SNE	<b>0.9633</b>	<b>0.9601</b>	<b>0.9551</b>	494.60
	UMAP	0.9586	0.9582	0.9382	107.00
	TriMap	0.9593	0.9589	0.8011	<b>95.00</b>
	scML	0.9185	0.9214	0.9219	109.45 ( $k_1=50$ ) / 69.05 ( $k_1=100$ )
MNIST	BH-t-SNE	0.8230	0.6196	0.5114	524.00
	UMAP	0.9677	<b>0.9618</b>	0.8152	105.00
	TriMap	<b>0.9712</b>	0.9521	0.5100	<b>93.00</b>
	scML	0.9290	0.9252	<b>0.8564</b>	89.20 ( $k_1=50$ ) / 58.53 ( $k_1=100$ )
FMNIST	BH-t-SNE	<b>0.8230</b>	0.6196	0.5114	528.00
	UMAP	0.7419	0.7066	0.5785	126.00
	TriMap	0.7383	<b>0.7070</b>	0.5207	<b>93.00</b>
	scML	0.7476	0.7049	<b>0.6076</b>	96.63 ( $k_1=50$ ) / 61.19 ( $k_1=100$ )
AG's News	BH-t-SNE	0.9645	0.7426	0.5940	506.00
	UMAP	0.9848	0.9848	0.9904	223.00
	TriMap	0.9775	0.9629	0.9761	128.00
	scML	<b>0.9943</b>	<b>0.9942</b>	<b>0.9944</b>	<b>62.13</b> ( $k_1=50$ ) / 31.64 ( $k_1=100$ )